NTNU – Trondheim
Norwegian University of
Science and Technology

An Experimental Study of the Jet in Cross-Flow in Fully Developed Turbulent Channel-Flow

Anna Nina Knutsen

NTNU

Norwegian University
of Science and Technology

Department of Energy
and Process Engineering

MASTER THESIS

Name: Anna Knutsen

Spring 2015

Experimental study of the jet in cross flow in fully developed turbulent channel flow

Background and objective

Transverse jets are found everywhere. They are observed when exhaust gases flow out of a chimney into the atmosphere and bent by the wind, as a method of fuel injection in combustion systems, and effusion cooling in gas turbine combustors where air flows through a series of small holes and bends to form a curtain of air which ensures the material does not reach their melting points (Did you know that when you fly a plane the combustor runs hotter than the melting point of the metal?). Despite its common use in engineering applications it has a very complex flow structure. In the near field it is comprised of complex vortex structures (hairpins and rollers), and in the far field a trailing vortex pair similar to that generated from the wing tips of an airplane. Although the mean structure is understood the turbulent structure is not and is therefore difficult to model using CFD. The aim of this project is to study the structure jet in cross flow in fully developed tubulent channel flow to see how the turbulent structure evolves and what effect free stream turbulence has on the scaling (if any).

The student will carry out the following tasks:
- Measure the trajectory of the jet for different scaling parameters.
- Make detailed flow visualisations and velocity measurements using PIV
- Process and anlyse the data to a level of quality of an international conference
- Compare the results with existing theory and report new findings

Within 14 days of receiving the written text on the master thesis, the candidate shall submit a research plan for his project to the department.

When the thesis is evaluated, emphasis is put on processing of the results, and that they are presented in tabular and/or graphic form in a clear manner, and that they are analyzed carefully.

The thesis should be formulated as a research report with summary both in English and Norwegian, conclusion, literature references, table of contents etc. During the preparation of the text, the candidate should make an effort to produce a well-structured and easily readable report. In order to ease the evaluation of the thesis, it is important that the cross-references are correct.

In the making of the report, strong emphasis should be placed on both a thorough discussion of the results and an orderly presentation.

The candidate is requested to initiate and keep close contact with his/her academic supervisor(s) throughout the working period. The candidate must follow the rules and regulations of NTNU as well as passive directions given by the Department of Energy and Process Engineering.
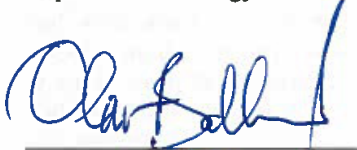
Risk assessment of the candidate's work shall be carried out according to the department's procedures. The risk assessment must be documented and included as part of the final report. Events related to the candidate's work adversely affecting the health, safety or security, must be documented and included as part of the final report. If the documentation on risk assessment represents a large number of pages, the full version is to be submitted electronically to the supervisor and an excerpt is included in the report.

Pursuant to "Regulations concerning the supplementary provisions to the technology study program/Master of Science" at NTNU §20, the Department reserves the permission to utilize all the results and data for teaching and research purposes as well as in future publications.

The final report is to be submitted digitally in DAIM. An executive summary of the thesis including title, student's name, supervisor's name, year, department name, and NTNU's logo and name, shall be submitted to the department as a separate pdf file. Based on an agreement with the supervisor, the final report and other material and documents may be given to the supervisor in digital format.

☒ Work to be done in lab (Water power lab, Fluids engineering lab, Thermal engineering lab)
☐ Field work

Department of Energy and Process Engineering, 14. January 2015

Olav Bolland
Department Head

James Dawson
Academic Supervisor

Research Advisor:

Abstract

In this study a transient air jet in a fully developed turbulent channel flow has been studied. The main objective has been to see how the behaviour of the jet has been effected by the turbulent channel flow.

The flow in the channel was first investigated through measurements with a Pitot static probe. A jet was then processed and inserted into the channel. Measurements of the resulting flow field were performed with a Pitot rake and a 5-hole Pitot probe. The results of these measurements have been analysed and compared to results from previous studies.

The velocity contours based on the results from the Pitot rake have proven to lack essential information about the jet in cross-flow flow field. The main feature of the flow field of the jet in cross-flow, the counter rotating vortex pair, was for instance not visible in the results collected with the Pitot rake. The results from the 5-hole Pitot probe showed a much better ability to capture the features of the complex flow field resulting from the jet in cross-flow.

Based on the results from this study, it does not seem that the turbulence have had a great impact on the development jet in cross flow. The development of the jet trajectory fits scaling laws found in previous studies. An increased vertical velocity component in the flow field and a delay in the development of the counter rotating vortex pair were noted as areas where the results from the turbulent channel differ from the results from previous studies [1].

Contents

List of Figures

List of Tables

Nomenclature

Symbols

Symbol	Unit	Description
J	-	Momentum flux ratio between jet and cross flow
ρ	kg/m^3	Density
Re	-	Reynolds number
d	m	Diameter
ν	m^2/s	Kinematic viscosity
V_r	-	Velocity ratio between jet and cross flow
x_{bp}	m	Branch point
l	m	Global length scale, high Re
m	kg/s	Mass flow
Γ	m^2/s	Circulation of one vortex in the CVP
c_x	-	Constant
$2R$	m	Separation between vortex cores
J	kg/s	Impulse per unit length
t	s	Time
A	-	Scaling constant
m	-	Scaling constant
U	m/s	Velocity
δ^*	m	Displacement thickness
$u(y)$	m/s	Local mean velocity
$\dot{m}$	l/min	Mass flow
A	m^2	Area
g	m/s^2	Gravity constant
z	m	Elevation of the point above a reference plane
p	Pa	Pressure
P	Pa	Pressure
Cp_θ	-	Pressure coefficient

Continued on next page

Symbol	Unit	Description
θ	°	Roll angle
ϕ	°	Yaw angle
h	m	Height

Subscript/superscript

Symbol	Description
∞	Cross-flow property
j	Jet-flow property
stag	Stagnation
stat	Static
θ	Roll angle, theta
ϕ	Yaw angle, phi
avg	Averaged
hg	Mercury
dyn	Dynamic

Chapter 1

Introduction

1.1 Jet in cross-flow

As the name implies, the term "jet in cross-flow" (JICF) refers to a jet of
fluid flowing from an orifice with an angle into a cross-flow. There are many
variations of the jet in cross-flow, depending on the nozzle exit shape and
size, the exit angle of the jet, the cross-flow properties, etc. The schematic
sketch in figure 1.1 shows the principle of a circular jet interacting with the
cross-flow over a flat plate. As the cross-flow passes the jet, it will bend in
the direction of the flow.
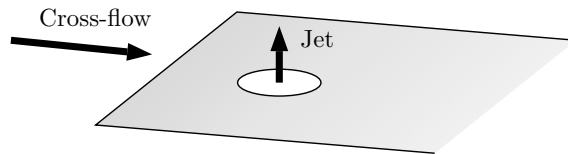
Figure 1.1: Principle sketch of the jet in cross-flow.

The jet in cross-flow has been studied thoroughly in experimental, compu-
tational and theoretical studies through the years both due to its frequent
occurrence in environmental and engineering devices and because of its fun-
damental significance as a turbulent flow [3].
Examples from environmental occurrences of the JICF include volcanic
plumes, large fires and chimney smoke, for which the bypassing wind is
working as the cross-flow. The transverse flow is affecting the spread of
ashes and smoke, and also the height to which the plume is rising, see fig-
ure 1.2(a).

As for engineering devices, jets in cross-flow are common in air-breathing engine systems, such as dilution air jets, and fuel and air mixers. Figure 1.2(b) shows a schematic diagram of a combustion section of a gas turbine engine with primary and dilution air jets which are injected transversely into the combustion chamber. The air jets in the primary zone are used to adjust the air-to-fuel ratio, which results in controlling the emissions of nitrogen oxide, NO_x. The dilution air jets have the purpose of cooling the combustion flow to an acceptable temperature before entering the turbine section of the engine [2].

Another engineering device where JICF is found is in the cooling system of gas turbine blades. In gas turbines the efficiency is increasing with increasing inlet temperature, and as a consequence of this the inlet temperature of today's turbines exceed the melting temperature of the turbine blades. Arrays of transverse air jets on the blades are used to film cool the material such that it does not melt.

A common goal for the jet in cross-flow is enhanced mixing or dispersal, as the jet in cross-flow has superior mixing characteristics compared with a free jet. For the film-cooling jets however, it is desired that the jets penetrate the flow as little as possible and rather follow the surface of the blades. Other industrial applications where the jet in cross-flow is found are thrust vector control of high speed aircraft and in rocket engine systems.
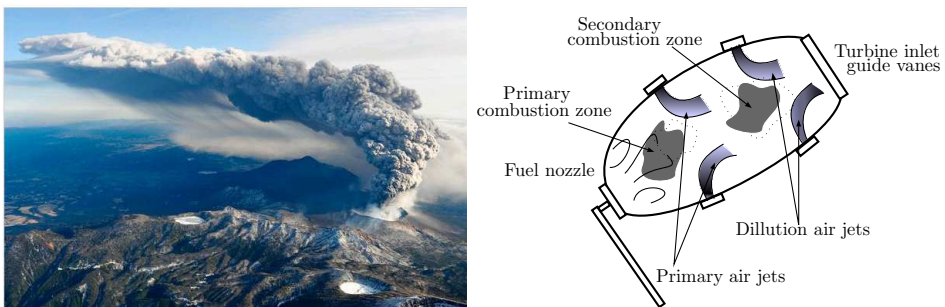
Figure 1.2: Occurences of the JICF in nature and engineering devices. (a) Volcanic plume from the Shinmoedake peak in Japan. Photo Kyodo/Reuters. (b) Schematic sketch of a combustion section of a gas turbine engine [2].

1.2   Flow characteristics

To describe the behaviour of the jet in cross-flow, the subscripts j and ∞ are used. Thus ρ_j and ρ_∞ are density of the jet and cross-flow respectively, and U_j and U_∞ are the velocities. These parameters are used to define the momentum flux ratio and the Reynolds number for incompressible transverse jets [3]:

$$J = \sqrt{\frac{\rho_j U_j^2}{\rho_\infty U_\infty^2}} \qquad (1.1)$$

$$Re_j = \frac{U_j d_j}{\nu_j} \qquad (1.2)$$

If the densities of the jet and the cross flow are equal, the momentum flux ratio in equation 1.1 will simplify to the velocity ratio between the two flows:

$$V_r = \frac{U_j}{U_\infty} \qquad (1.3)$$

Former research [4] has shown that the development of the jet trajectory is primarily dependent on the non-dimensional parameters in equation 1.1 and equation 1.2. In the case of low velocity ratios the jet will bend directly above the exit of the jet, whereas for high velocity ratios the jet trajectory will penetrate higher into the cross flow before it bends and thus it will dominate the flow topology to a greater extent [5].
The interaction between the jet and cross-flow results in a complex flow field consisting of several vortex structures, especially in the near field of the jet [6].
The branch point, x_{bp}, in equation 1.4 is used to determine the transition point from the near field to the far field of the jet in cross-flow [1].

$$x_{bp} = 0.2 V_r^2 d_j \qquad (1.4)$$

The instantaneous jet structure is very different from the averaged flow field [7]. While the instantaneous velocity picture is unsteady, the average field is characterized by a smooth shape. For instance are jet shear-layer vortices observed at the windward side of the jet. These are highly unsteady and

3

cannot be seen in any time-averaged results.

In the far field of the jet the flow is dominated by a counter rotating vortex pair (CVP), as seen in figure 1.3 [6].
The origin of the formation of the CVP has been discussed, and an early theory was that the shear layer instabilities of the jet led to a roll-up of vorticity in the near field of the jet had an important role [2]. Recent numerical studies, however, have demonstrated that the shear layer vortices are not necessary to be able of producing the CVP [3] [8]. These studies demonstrated that a steady simulation of a 3D flow field is capable of producing the CVP, and consequently the shear layer vortices are not necessary to initiate the formation of the CVP. It is on the other hand agreed upon that the vortex rings at the inlet influence the vorticity of the CVP [6] [2]. The CVP has a great impact on the flow picture, such as through an enhanced mixing in a JICF compared to a free jet [7]. As the velocity ratio increases, the formation of the CVP is moved further downstream from the jet exit [7].
Other vortex structures observed in the JICF are horseshoe vortices and wake structures. The horseshoe vortices form upstream of the jet and wrap around the jet exit, while the wake structures are created leeward side of the jet and remain in the flow far downstream [7].
At velocity ratios 5 and smaller, the jet in cross flow is in a different regime. The wall effects are more important, and the flow structures are behaving differently, thus the resulting flow field at these low velocity ratios will differ from the flow field described above with the CVP as the main feature of the flow [7].

1.2.1   Scaling of the jet

The jet trajectory describes to which extend the jet fluid penetrates into the cross-flow. Various methods have been used to define the jet trajectory, including the position of the local velocity maxima, the local scalar maxima, the vorticity maxima, and the time averaged streamline originating from the jet exit [3].
As the jet is deflected, the velocity of the jet decays rapidly to values comparable to the cross flow velocity, and at around $x/d_j = 15$ the jet velocity is found to have decayed to such a degree that it is experimentally difficult to locate the maximum and thus the jet center line [9].
The vortex curve is the projection of the center of either vortex onto the symmetry plane. Since the CVP is the dominating feature of the flow,
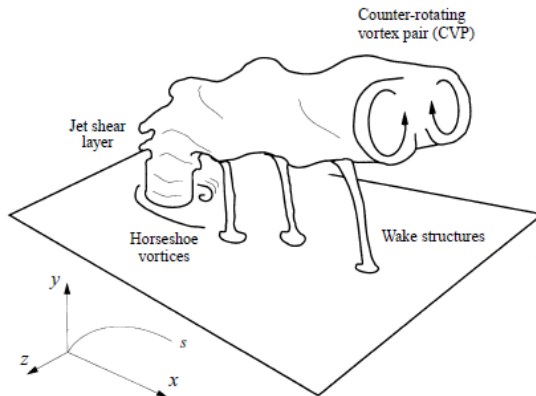
Figure 1.3: The known vortical structures of the jet in cross-flow.

the vortex curve can be determined much further downstream than the jet center line [9]. Because of this, it is the definition of the jet trajectory based on the vortex curve that has been utilized in this study.

The scaling of the near field and the far field have been found to differ. $V_r^2 d_j$ was proposed by [10] to collapse the trajectory in the near field of the jet up to eight jet diameters from the jet exit [3]. In order to collapse the jet trajectory in the far field the length scale $V_r d_j$ was proposed by [11].

[12] demonstrated that that for the far field, both the jet trajectory, y, and the vortex spacing, $2R$, vary with the downstream distance x to a power close to one third.

This power law can be derived by looking at the limiting situation where the jet momentum flux, $m_j U_j$, is held constant as the mass flow and jet diameter go to zero, while U_j increases. Towards limit of this situation a point source of normal momentum is approached. For high Reynolds number flows, where the viscosity does not have an importance compared to the momentum, the only global length scale for the described flow is [13]:

$$l = \left(\frac{m_j U_j}{\rho_\infty U_\infty^2} \right)^{1/2} \tag{1.5}$$

In the far field the CVP is moving with, and are approximately aligned with the cross-flow. Thus, in a coordinate system moving with the cross-flow velocity, U_∞, the mean flow is close to being two-dimensional with the vortices dominating the flow picture.

The relation of the vertical velocity, dy/dt, the impulse per unit length, J,

5

the circulation of one vortex, Γ, and the separation of the vortex cores, $2R$, is given in equation 1.6 and 1.7:

$$\frac{\mathrm{d}y}{\mathrm{d}t} = \frac{c_1\Gamma}{R} \tag{1.6}$$

$$J = c_2\rho_\infty\Gamma R \tag{1.7}$$

where c_x is a constant.

When combining equation 1.6 and 1.7 we get:

$$\rho_\infty R^2\frac{\mathrm{d}y}{\mathrm{d}t} = c_3 P \tag{1.8}$$

In the far field ($x \gg l$) the flow is expected to be independent of l and therefore a similarity solution where R is proportional to y is expected to exist. Based on this assumption, equation 1.8 becomes:

$$c_4\rho_\infty y^2\frac{\mathrm{d}y}{\mathrm{d}t} = P \tag{1.9}$$

Equation 1.9 describes the flow generated by a line impulse of strength P. When solving for y, we get:

$$y = c_5\left(\frac{J}{\rho_\infty}\right)^{1/3}t^{1/3} \tag{1.10}$$

Equations 1.6 and 1.7 then become:

$$R = c_6\left(\frac{J}{\rho_\infty}\right)^{1/3}t^{1/3} \tag{1.11}$$

$$\Gamma = c_7\left(\frac{J}{\rho_\infty}\right)^{2/3}t^{-1/3} \tag{1.12}$$

$x = U_\infty t$ is used to return to the original, stationary coordinate system. Also note that $J = m_j U_j/U_\infty$. Equation 1.10 then yields:

$$\frac{y}{l} = c_5\left(\frac{x}{l}\right)^{1/3} \tag{1.13}$$

and equations 1.11 and 1.12 become

$$\frac{R}{l} = c_6\left(\frac{x}{l}\right)^{1/3} \tag{1.14}$$

6

$$\frac{\Gamma}{U_\infty l} = c_7 \left(\frac{x}{l}\right)^{-1/3} \tag{1.15}$$

Equations 1.13-1.15 is expected to describe the flow fields of high velocity ratios for $x \gg l$.

When $\rho_j = \rho_\infty$, the length scale becomes $V_r d_j$. For this case equation 1.13 becomes:

$$\frac{y}{V_r d_j} = c_5 \frac{x}{V_r d_j}^{1/3} \tag{1.16}$$

The far field the length scale, $V_r d_j$, suggested by [11] is recognized in equation 1.16.

The power law stating that the far field penetration of the jet varies with $x^{1/3}$ has been confirmed by several experimental studies [11]. The value of the exponent in the power law has been found to vary slightly around $1/3$. Equation 1.16 is thus often written as:

$$\frac{y}{V_r d_j} = A \frac{x}{V_r d_j}^m \tag{1.17}$$

with A and m being scaling constants. Values of m between 0.28 and 0.38 have been found to scale the trajectory. The value of A is found to vary between 1.2 and 2.6 [1].

The interval of values for m and A from experiments is quite big. One reason for this is that the definition of the jet trajectory can be defined in several manners as earlier discussed in this chapter. [11] has found that equation 1.17 is valid for $5 < V_r < 35$.

1.3   Motivation for present study

In most cases the JICF is studied in the free stream of a cross flow where the turbulent intensity goes to zero, for example in the free stream of a wind tunnel. There are therefore limited information about the effects of turbulence on both the time averaged and the instantaneous behaviour of the jet.

The main objective of this study is to investigate the JICF in a fully developed channel flow where the turbulent fluctuations and wall effects are significant.

The scaling of the jet trajectory in the turbulent channel flow will be studied and compared to the existing scaling laws discussed in chapter 1.2.1. The behaviour of the different velocity components downstream of the jet will

be discussed and compared to existing results from studies where the jet is placed in the free-stream, and the turbulent intensity is small.

Measurements will be performed with a Pitot rake and a 5-hole Pitot probe in order investigate the resulting flow field of the JICF. Another objective of the study is to see how well fit these measuring devices are to accurately capture the complex flow field of the jet in cross flow.

Chapter 2

Apparatus

2.1 The channel

Figure 2.1 shows the channel used for the experiments situated in the fluid mechanics laboratory at the Norwegian University of Science and Technology. The flow investigated is categorized as closed channel flow, where the flow is entirely in contact with rigid boundaries, and the height to width ratio of the channel is small. The height of the channel was adjusted to be constant 25.0 cm, as a zero pressure-gradient flow was desired, and the width of the channel was 140 cm.

An increased turbulence in the flow was obtained by floating elements placed on the channel floor. Figure 2.3 shows a sketch of the floating elements and their dimensions, and figure 2.2 shows a sketch of the channel with the jet.

2.1.1 Static pressure

When the measurements with the Pitot rake was performed, the static pressure was first measured with a single Pitot static probe, as the rake did not have any static pressure ports. A test was performed to see if the static pressure was varying across the vertical direction of the channel. The results (figure 2.4) shows that compared to the total pressure, the static pressure does not vary much, especially in the middle section of the channel. The variance in static pressure visible in the lower section of the channel in the results in figure 2.4 might be caused by the component of vertical velocity in this section (see figure 2.6), as this velocity will influence the pressure felt by the static pressure tap.

Figure 2.1: The wind tunnel used for the experiments.
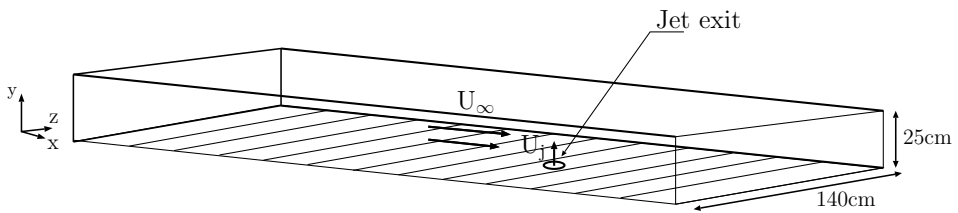
Figure 2.2: Schematic sketch of the channel used for the experiments.
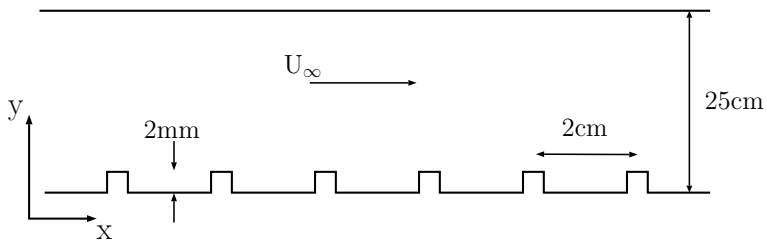
Figure 2.3: Sketch of the roughness elements on the channel floor.

Based on these results, it is concluded that it is acceptable to assume that the static pressure is constant throughout the vertical section of the channel, and that a single measurement with the Pitot static probe was sufficient. The mean of the static pressure was found in the middle of the channel,

and this is where the measurements with the static Pitot probe was done before every measurement with the Pitot rake.
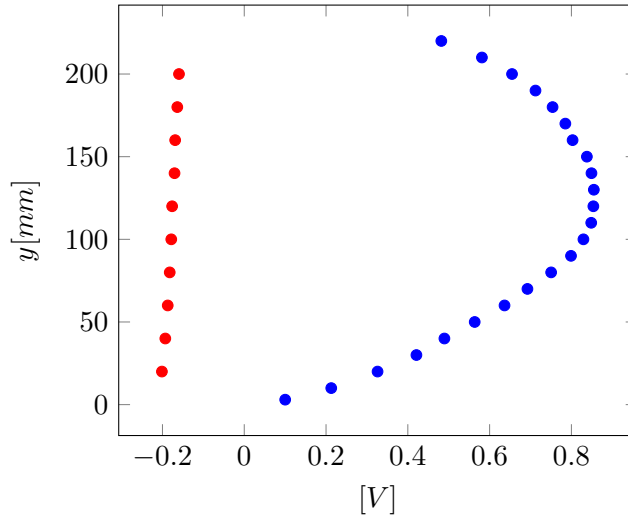
Figure 2.4: Static pressure signal (•) plotted against the total pressure signal (•) from a static Pitot probe.

2.1.2 The cross-flow

Before the jet was inserted into the channel, the cross-flow was investigated. A vertical velocity profile of the test section was measured with the Pitot rake and the 5-hole Pitot probe in the same downstream position as the jet was to be inserted.

The measurements with the Pitot rake were taken from the center of the channel, at z = 0 cm, to z = 55 cm. Figure 2.5 displays the resulting velocity field from the test with the Pitot rake. The velocity is scaled with the inlet velocity, in this case 10.01 m/s. An increasing velocity from the lower part of the region to the center is observed before the velocity again starts to decrease due to the effects of the channel ceiling. The velocity is increasing in a uniform manner throughout the span wise direction (z-direction) of the channel.

The measurements with the 5-hole Pitot was taken at z = 6 mm. Figure 2.6 shows a section of the channel with the cross-flow measured with the 5-hole Pitot probe. The total velocity and the velocity in the x-direction of the

channel is overlapping almost perfectly. The span wise velocity component U_z is close to zero throughout the measured domain, with a maximum deviation from zero of -0.15 m/s. The vertical velocity component has somewhat higher values towards the channel floor ($0.32 m/s$ at most). This fits well with what is expected from the behaviour of the different velocity components of the flow close to the channel floor.
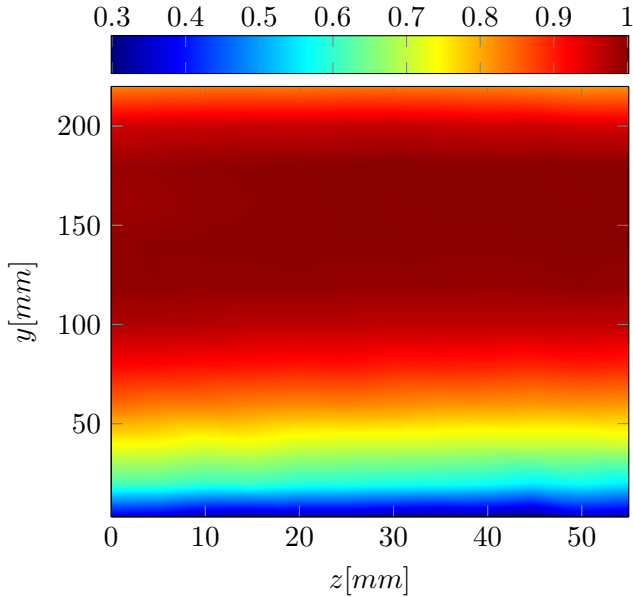
Figure 2.5: Velocity field measured by the rake, no jet.

2.1.3 Self similarity of the channel flow

In order to get a further understanding of the channel flow, a single Pitot static probe was used to do measurements at various positions in the channel to check if the flow was self-similar. Figure 2.7 shows the results of the measurements done at x = 2 m downstream from the channel inlet for different inlet velocities.

In figure 2.7(b) the profiles have been collapsed with the inlet velocity, U_∞, and the displacement thickness, δ^*. The displacement thickness is the distance a streamline just outside the boundary layer of the flow is displaced away from the wall compared to the inviscid solution [14], and is defined as:
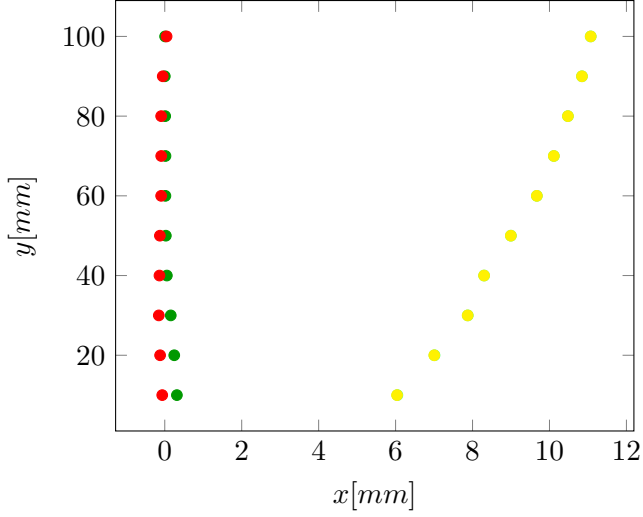
Figure 2.6: The different velocity components in a section of the channel measured with the 5-hole Pitot of the cross-flow only: ● : U, ● : U_x, ● : U_y, ● : U_z.

$$\int_0^\infty u(y)dy = \int_{\delta^*}^\infty U_\infty dy \to \delta^* = \int_0^\infty (1 - \frac{u(y)}{U_\infty})dy \qquad (2.1)$$

Where U_∞ is the free-stream velocity, and $u(y)$ is the local mean velocity at a position y from the wall.

The integral of the velocity in equation 2.1 was found using the trapezoidal method in MATLAB, as a functional expression is not available for the velocity profiles and thus the integral function in MATLAB could not be used.

The different graphs collapse well when scaled, with only small offsets, and is thus found to be self-similar.

2.2   The jet

The jet that was used to perform the experiments has an exit diameter of 5 mm. Inside the jet there was a grid for smoothing the flow before the exit. The jet is pictured in figure 2.8, both before and after inserted in the channel.
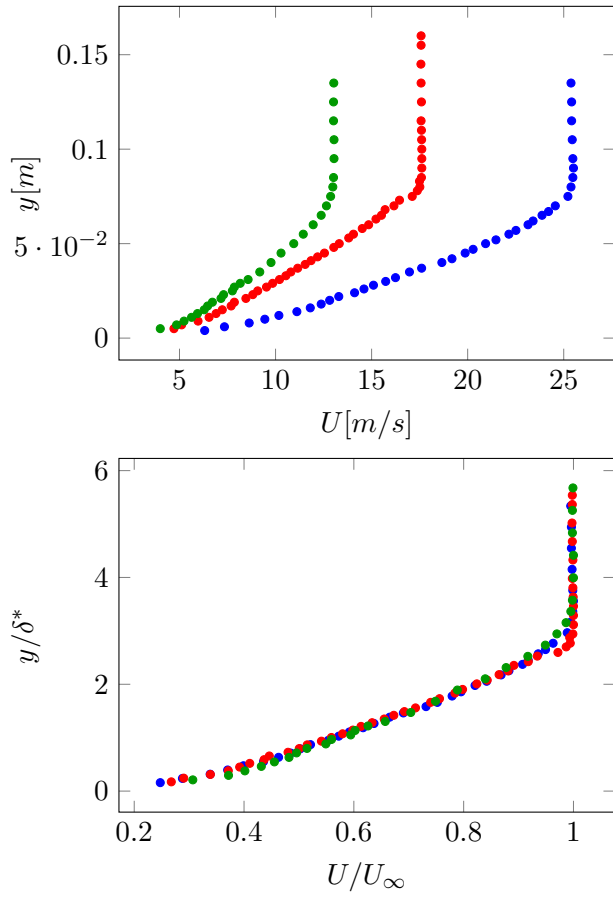
Figure 2.7: Channel flow at x = 2 m downstream from the channel inlet. Before (a) and after (b) scaling.

Before the jet was ready to be placed in the tunnel it needed some processing. The jet consisted of two pieces which were to be screwed together by aluminium threads. As these had been torn down due to wear, it was not possible to seal the jet properly. As a solution the threads were completely grinded away, and the jet was put together and sealed with Loctite sealant and screws. The upper part of the jet was then extended such that it had the same height as the thickness of the channel floor. The jet could then easily be inserted into the channel such that the jet exit was levelling with the channel floor and thus the jet itself would not disturb the flow (figure 2.8b). As it was desired to investigate the jet in fully developed channel flow, the jet was placed far downstream of the inlet of the channel, at x = 3.3m, where the flow was checked to be fully developed.
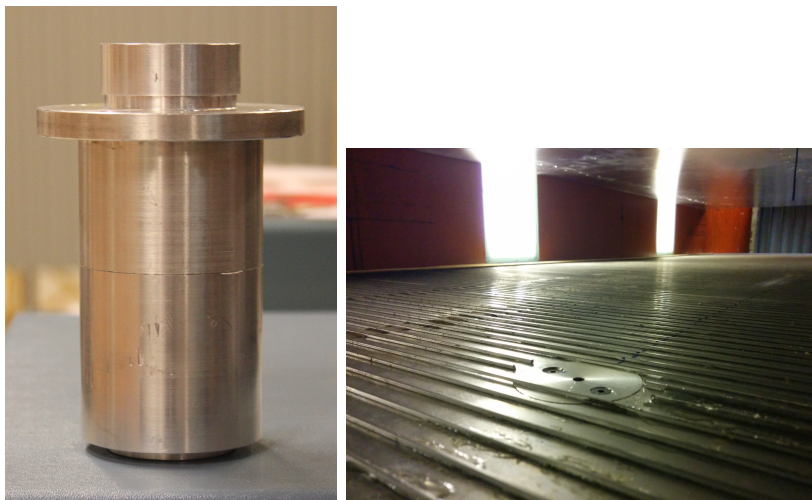
Figure 2.8: The jet before (a) and after (b) inserted in the channel.

2.3   Mass flow controller

The mass flow controller used for the experiments was from the ALIGAT Scientific MCR-series. A hose connected to an air supply was fastened to the inlet connection port of the mass flow controller, and another hose was connecting the outlet port to the bottom of the jet. The mass flow controller had a display screen were the mass flow rate of the air could be set in standard liters per minute. To get the correct jet velocity needed for

the experiments, equation 2.2 was used:

$$\dot{m}\ [\text{l/min}] = U_j\ [\text{m/s}]\ A_j\ [\text{m}^2]\ *60[\text{s/min}]\ *1000[\text{l/m}^3] \qquad (2.2)$$

During the measurements the jet velocity varied from 50 m/s to 102 m/s. This gives a maximum Mach number of 0.297. Compressible effects of the flow are small up to a Mach number of 0.3 [15], and will not be considered in this study.

2.4   Pitot static probe

The Pitot static tube is used to measure flow velocity. It is based on the principle that the flow velocity can be determined by the difference in stagnation pressure and static pressure. There is a stagnation pressure tap in the front, and one or more static pressure tap on the side of the tube to measure the different pressures.

The kinetic energy in the flow converts to potential energy at the stagnation point in front of the Pitot static probe when aligned in the flow, and results in an increase in the pressure (to stagnation pressure). For compressible flow of Mach number less than 0.3, Bernoulli's principle in equation 2.3 reduces to equation 2.4 when choosing point 1 as an undisturbed point of the streamline, and point 2 as the stagnation point, and with $z_1 = z_2$ and $U_2 = U_{stag} = 0$ [16].

$$\frac{U_1^2}{2g} + z_1 + \frac{p_1}{\rho g} = \frac{U_2^2}{2g} + z_2 + \frac{p_2}{\rho g} \qquad (2.3)$$

$$U = \sqrt{\frac{2(p_{stag} - p_{stat})}{\rho}} \qquad (2.4)$$

A Pitot static tube aligned in the flow direction was used to examine the channel-flow, for calibration of the pressure transducer and to get a reference value for the static pressure while doing measurements with the Pitot rake. The outer diameter of the Pitot-static probe used in the experiments was 4 mm, and the inner diameter was 1 mm. The tube had a rounded tip, which will influence the flow less than a flat tip and helps to prevent separation [17].

2.5 Pitot rake

The Pitot rake was built in the lab, and is pictured in figure 2.9. it consists of 16 pressure ports aligned in the row, 5 mm apart. The total area covered by the rake was 75 mm. The inner diameter of the probes were 1.5 mm, while the outer diameter was 2 mm.

The rake was aligned in flow direction, first by a visual alignment, then adjusted with a digital level to make sure that each of the probes were aligned horizontally in the flow. A test was performed with the Pitot rake before the jet was inserted to the channel, see chapter 2.1.2.

A manual traverse system was used to raise and lower the rake during the measurements.

Figure 2.9: The pressure rake.

2.6 5-hole Pitot probe

A limitation of the single hole Pitot probe is that it cannot distinguish between the different velocity components of the flow. Also the pressure difference will decrease if the pressure tap is not aligned in the flow direction, and thus the resulting velocity measured by the rake will not be the actual flow velocity. In a complex flow field such as the one related to the jet in cross-flow, the angle of the flow direction has big local variations, and this makes it hard to get proper measurements with a single-holed Pitot tube or a Pitot rake.

The principle of the 5-hole Pitot is the same as for a normal Pitot probe, the velocity can be calculated by looking at the difference of the stagnation pressure and the static pressure, as described in chapter 2.4. The difference is that the 5-hole Pitot has two pairs of symmetrically placed pressure taps inclined in different angles with respect to the incoming flow. The concept

of the probe is to be able to measure the magnitude and direction of the flow based on the different pressures measured by the different taps.

Two general methods exist for doing measurements with the 5-hole Pitot probe; the nulling and the non-nulling method. The nulling method is time consuming and requires an accurate traversing system. The data acquisition time is long, especially if the probe is small and has a long response time. For this method, the probe has to be pitched and yawed until the different pressures are equal at each measuring point. The probe is then angled in the flow direction, and the pitch and yaw angle can be noted [18].

The non-nulling method has the disadvantage that it requires a somewhat complicated calibration process and post processing. The data acquisition time is, however, shortened drastically. Therefore this method was chosen for this project.

2.6.1 Calibration

The calibration process in the non-nulling method was performed as described in [18]. The probe with its nomenclature is sketched in figure 2.10. For the calibration process a flow with a constant velocity and direction was needed. A rectangular wind-tunnel in the second floor of the fluid mechanics lab at NTNU was used for this purpose. The probe was mounted on an adapter which made it easy to vary the yaw, ϕ, and roll, θ, angles of the probe with respect to the incoming flow. In [18] the yaw and pitch angles were varied, but the available adapters made it more convenient to vary the roll angle (as done in [19]).

The probe was then angled around a point (the head of the probe always remained at the same position) for a series of pitch and roll angles. A picture of the probe mounted in the channel is shown in figure 2.11. The tap on top of the probe (figure 2.11) was put there to easier control the roll angle. A digital level was to find the correct angles, with and error of ± 0.1 degrees.

The initial position of the probe was at $\phi = \theta = 0$ with regards to the incoming flow. As the 5-hole Pitot probe did not have any static pressure taps, and the static pressure was necessary for the calibration, a single Pitot static probe was used to measure the static pressure before starting the sampling with the 5-hole Pitot probe. Then the P1 to P5 was measured. The pressure measured from P5 at the initial position was the stagnation pressure, P_{stag}. The velocity of the flow during the calibration was 10.4 m/s, a value between the cross-flow velocity and the highest expected value in the center of the vortex cores.
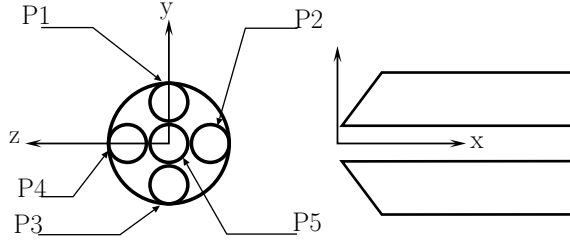
Figure 2.10: Schematic sketch of the 5-hole Pitot.
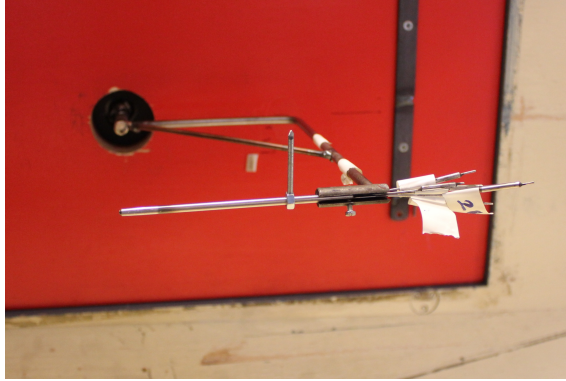
Figure 2.11: Set-up for the calibration of the 5-hole Pitot probe.

The the yaw and roll angles were varied over a matrix of different angles, and the pressures P1-P5 were recorded at each position. The yaw angles were chosen to be: 1.5, 3, 5, 10, 15, 20, 25, 30, 35 and 40°, while the roll angle was changed in steps of 15°, where 0°= 360°. The resulting data was then reduced by the standard accepted non-dimensional grouping in the following equations:

$$Cp_\theta = \frac{P_3 - P_1}{P_5 - P_{avg}} \tag{2.5}$$

$$Cp_\phi = \frac{P_2 - P_4}{P_5 - P_{avg}} \tag{2.6}$$

$$Cp_5 = \frac{P_5 - P_{stat}}{P_{stag} - P_{stat}} \tag{2.7}$$

$$Cp_{avg} = \frac{P_{avg} - P_{stat}}{P_{stag} - P_{stat}} \tag{2.8}$$

where $P_{avg} = 1/4(P_1 + P_2 + P_3 + P_4)$.

Three-dimensional functions of the coefficients where achieved by plotting the coefficients from equations 2.5-2.8 against the angles and interpolating between the points. The resulting functions are shown in figures 2.12 and 2.13.

The curve fitting tool in MATLAB was used with the interpolate cubic method to fit the data and make functions that could later be used to determine ϕ and θ for the measurements done with the JICF. This interpolation reduced the effect of bad calibration points and asymmetries in the probe. The obtained graphs of Cp_5 and Cp_{avg} look smooth for yaw angles up to approximately $\phi = 20°$. Good quality of the calibration and the probes ability to measure the different flow angles is indicated by a smooth graph, thus the 5-hole Pitot probe is suitable to measure incoming flow angles up to 20°.

For the roll angle, θ, Cp_θ and Cp_ϕ were plotted against the periodic functions sin and cos to avoid interpolation errors between 0°and 360°. Both the sin and cos functions were plotted to get an explicit solution for θ.

2.6.2 Measurements with the 5-hole Pitot

For the post-processing of the data from the measurements of the JICF with the 5-hole Pitot probe, the following steps were followed in MATLAB:

1. The Cp_ϕ and Cp_θ were first calculated from the measured values $P1 - P5$.

2. ϕ and θ were then determined using the interpolated functions displayed in figure 2.12.

3. Cp_5 and Cp_{avg} was determined using the functions displayed in figure 2.13.

4. The static pressure and the stagnation pressure were calculated using the following equations:

$$P_{stat} = \frac{Cp_5 P_{avg} - Cp_{avg} P5}{Cp_5 - Cp_{avg}} \tag{2.9}$$

$$P_{stag} = P_{stat} + \frac{P1 - P_{stat}}{Cp_5} \tag{2.10}$$

a)

b)

c)
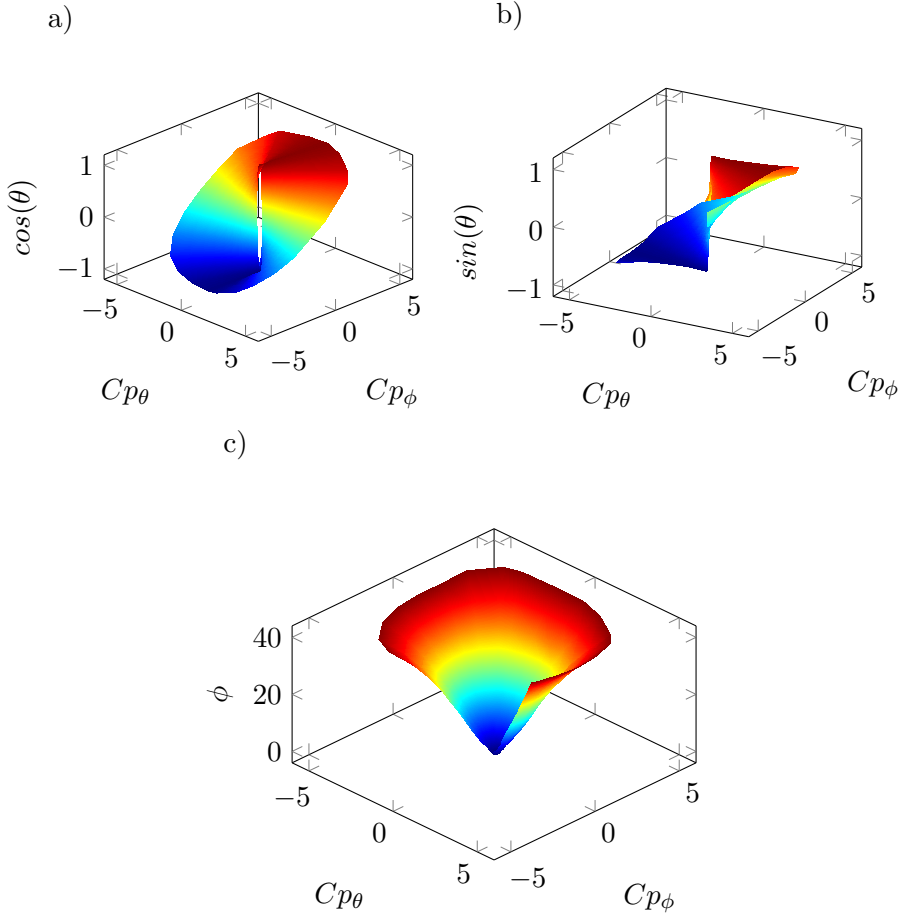
Figure 2.12: $cos(\theta)$ (a), $sin(\theta)$ (b) and ϕ (c) plotted against Cp_ϕ and Cp_θ.

5. The total velocity was calculated using:

$$U = \sqrt{\frac{2(P_{stag} - P_{stat})}{\rho}} \quad (2.11)$$

6. A transformation from spherical to Cartesian coordinates was performed:

$$U_x = U cos(\phi) \quad (2.12)$$

$$U_y = -U sin(\theta) sin(\phi) \quad (2.13)$$

21

a)

b)
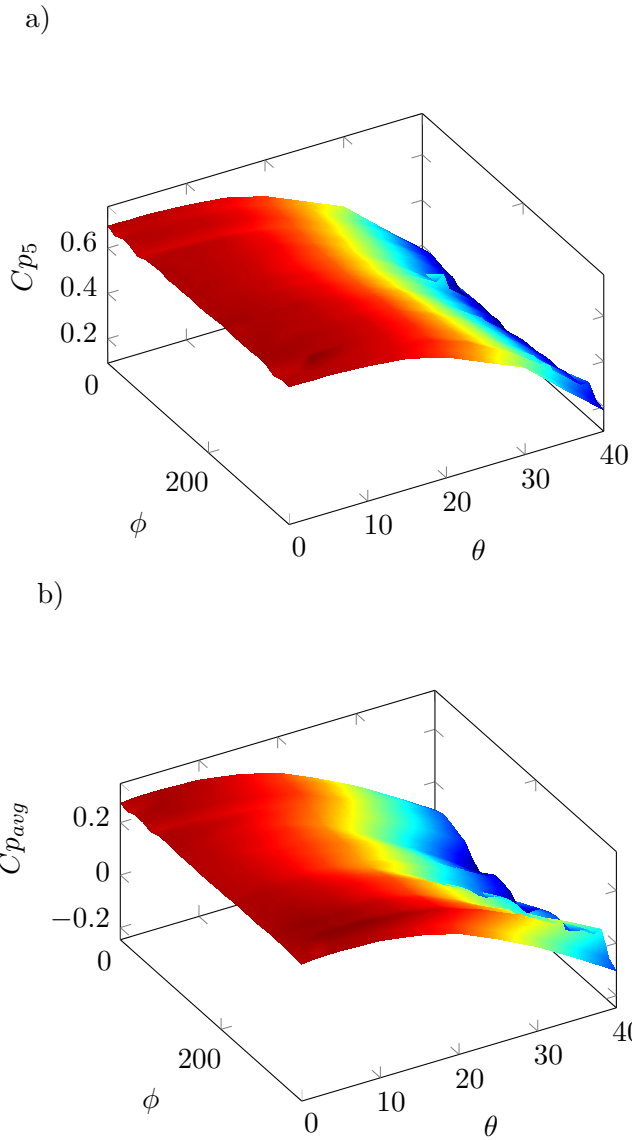
Figure 2.13: Cp_5 (a) and Cp_{avg} (**b**) plotted against θ and ϕ.

$$U_z = -U cos(\theta) sin(\phi) \tag{2.14}$$

The probe used for the experiments had an outer diameter of 4 mm. Each of the pressure holes had an inner diameter of 1 mm. The previously men-

tioned tap fastened to the probe was kept to make sure that hole number one ($P1$) was pointing upwards at all times. This was especially important because the probe was manually moved during the measurements of the JICF. Even though this displacement was done very carefully, it was necessary to have a way to verify that the position of the probe was right. The 5-hole Pitot probe, both before and after inserted in the channel, is pictured in figure 2.14.
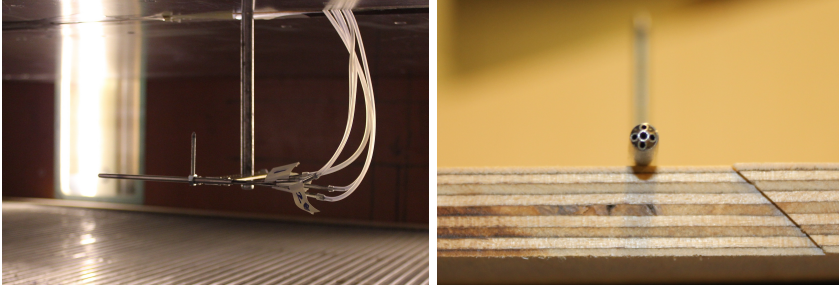
Figure 2.14: The 5-hole Pitot probe before (a) and after (b) inserted into the channel.

2.6.3 Traverse system

There was no automatic traverse systems that fitted into the channel, therefore a manual traverse system for the 5-hole Pitot probe was made. The objective was to make this as accurate as possible. A one-dimensional manual traverse was used for movement in vertical direction. To be able to accurately shift the probe in horizontal direction, the frame pictured in figure 2.15 was made. By fixing the probe in the end of the device (on the left side in figure 2.15), the medal rod from the traverse could be fastened to any of the holes, and thus the distance between the center of the channel and the probe could be controlled.

To be able to align the probe accurately in the cross-flow direction every time it was shifted in span wise direction a digital level and an angle measuring device were used. The distance between the center of each hole in the frame was 6 mm and there was 15 holes, hence the closest z-position to the center that was possible to measure was at z = 6 mm and the position furthest away was at z = 90 mm.

Figure 2.15: the manual traverse device used to move the 5-hole Pitot in horizontal direction.

2.7 Manometer

The manometer measures the pressure using a liquid column, in this case mercury. Two tubes, one connected to the static pressure gate of a Pitot tube and one to the stagnation pressure gate, are attached to the manometer. The stagnation and static pressure will be exerted on each side of the liquid column. As the stagnation pressure is higher, this will cause a rise of the mercury column. From the rise of the mercury, h_{hg}, one can calculate the dynamic pressure of the flow:

$$p_{dyn} = p_{stag} - p_{stat} = \rho_{hg} g h_{hg} \qquad (2.15)$$

The manometer used in this study was Wilh. Lambrecht K6, type 655 manometer. It has an systematic accuracy of $\pm 1\%$ from the respective full scale value [20]. In addition comes the human error from reading of the value of the manometer. Due to the turbulence, the liquid column fluctuates slightly, and the average is taken at best ability by a visual estimate. In this study the manometer was used to calibrate the pressure transducer, see chapter 2.9.

2.8 Pressure scanner

A pressure scanner was configured to make it possible to connect the different tubes from the rake probes to one pressure transducer and thus easily change which probe is connected to the transducer. This made it possible

to increase the efficiency of the measurements with the rake. The pressure scanner used was a "påk SCANIVALVE CONTROLLER" [21].

It was possible to connect up to 48 inlet tubes and one outlet tube to the pressure scanner. The outlet tube was always connected to the pressure transducer during the measurements. A manual controller managed which inlet tube that was linked to the outlet tube, and hence sent a pressure signal to the pressure transducer. For the rake measurements 16 of the inlet tubes were connected to the rake ports, and while doing measurements with the 5-hole Pitot, five inlet tubes were connected to the pressure scanner.

2.9   Pressure transducer

The pressure transducer makes an applied pressure into a measurable electrical signal through a linear relation. A manometer was used to calibrate the pressure transducer. During the calibration process the manometer and the pressure transducer were connected in parallel to a static Pitot probe which was placed in the channel. The applied pressure was changed in small steps by increasing the wind speed in the channel. The height of the liquid column in the manometer and the voltage signal from the pressure transducer was then registered, and a calibration constant was found by plotting the data from the measurements against each other and fitting a linear trend line. The transducer used for the experiments had a pressure constant of around 760 Pa/V. Over the period the experiments were performed, the calibration process was repeated multiple times to make sure that the constant used when transforming the voltage signal to pressure was correct.

The pressure transducer used in the experiments was a "Setra Systems, model 239 High Accuracy Pressure Transducer". It has an accuracy of $\pm$ 0.14 % and has a range of $\pm 750 mmH_2O$ (= 7354 Pa).

2.10   Data acquisition

Silicon tubes connected the pressure ports from the 5-hole Pitot probe and the pressure rake to the inlet channels of the "påk SCANIVALVE CONTROLLER" pressure scanner. Further the outlet tube of the pressure scanner was connected to the pressure transducer with another silicon tube. To increase the accuracy of the results, the pressure transducer was linked in series to an amplifier (produced in-house). An amplification of 20 was used when performing the measurements.

From the amplifier, the signal was sent to a National Instruments cDAQ-9174 data acquisition board, which was connected to a PC through a USB port. The incoming signals were then recorded by a National Instruments LabVIEW program running on the PC. The program made it possible to vary the sampling time and rate. The recorded data of the voltage signals was then transformed to pressure values and further evaluated in MATLAB.

2.11   Measurement locations

The locations of the measurement positions for the rake and the 5-hole Pitot probe varied from $6d_j$ to $70d_j$ downstream of the jet exit. The measurements taken with the Pitot rake close to the jet exit(at $x = 6d_j$, $8d_j$ and $10d_j$), did not give good results as the jet had not had sufficient time to be fully bent over by the cross-flow, and separation occurred when the jet flow hit the rake probes.

The rest of the measurement positions for the Pitot rake and the 5-hole Pitot probe is listed in table 2.1.

Pitot rake	5-hole Pitot probe
$10d_j$	$30d_j$
$20d_j$	$40d_j$
$30d_j$	$50d_j$
$40d_j$	$60d_j$
	$70d_j$

Table 2.1: Measuring positions downstream of the jet for the Pitot rake and the 5-hole Pitot probe.

The positions of the Pitot rake measurements are located closer to the jet than the 5-hole Pitot measurements. The reason for this is that the objective was to locate the CVP of the jet. When these where not observed in the beginning of the far field where they were expected to be fully developed, it did not seem likely hat the results of the Pitot rake would show the CVP further downstream from the jet. Thus the 5-hole Pitot probe was applied instead to get a better picture of how the flow was developing.

2.12 Grid size

The grid size used for the measurements varied from 5 mm to 12 mm, being more dense in the area where the cores was expected to be (based on equation 1.17).

For the 5-hole Pitot probe an average grid had 100 points, distributed over an area of around 60 cm^2. At each point five measurements were necessary to get the the pressure from all five holes in the probe. The sampling time was set to 15 seconds per point. Only the sampling time for one experiment with the rake was thus around 2 hours. In addition to this the traverse had to be moved manually between each point. Especially when this was done in the horizontal direction it took 1-2 minutes to make sure that the probe was aligned correctly in the flow. The flow was then given 10 seconds to settle for each time the traverse was moved. When including this, the total time for one experiment with the 5-hole Pitot probe was (optimally) around 3.2 hours.

The measurements performed with the rake was more efficient as the rake only had to be moved between every 16th measurement (due to the 16 probes), thus it was easier to get a higher resolution on the grid and to cover a bigger area. An average of 300 points were measured over an area of around 140cm^2. The sampling time was, also here, set to 15 seconds. Thus the total sampling time for the rake measurements were 75 minutes. When including time to move the rake and let the flow settle one measurement period was at around 100 minutes if everything went smoothly.

Chapter 3

Results

In the following chapter the results of the measurements are presented. All velocities are normalized by the free-stream velocity measured in the center of the channel before the jet flow is turned on. When performing measurements with the rake, the free-stream velocity was measured by a single Pitot static probe temporarily inserted in the channel at the same position as the Pitot rake. The Pitot static probe was also used to measure the static pressure.

As for the 5-hole Pitot, one measurement was done with each of the five pressure taps, and the different velocity components were calculated. By doing this, it was also convenient to verify that the probe was mounted correctly in the channel, as the flow in the middle of the channel is known to be parallel and hence the measured vertical and span wise velocities, U_y and U_z, should be close to zero. The free-stream velocities were all in the range between $U_\infty = 9.0$ m/s and $U_\infty = 10.6$m/s, for both the rake and the 5-hole Pitot measurements. The only exception was the measurements performed with the Pitot rake for the velocity ratio $V_r = 14$. In order to insure that the jet flow was incompressible, the cross-flow velocity for these measurements was adjusted down to 7.4 m/s, such that the jet velocity became 103.6 m/s. This gives a Mach number of 0.30.

The y- and z-axis for all figures with the jet present have been scaled by the global length scale $V_r d_j$. The color-scales for the figures in the categories have been standardized to make it easier to follow the development of the jet trajectory.

3.1 Pitot Rake

Measurements were performed for various locations downstream of the jet for a range of different velocity ratios. The different cases that was measured are listed in table 3.1, where x/d_j is the distance from the center of the jet exit nozzle to the measuring point.

$\mathbf{x/d_j}$	$\mathbf{V_r}$		
20	5	7	10
30	5	7	14
40	10		

Table 3.1: *The different velocity ratios for the measuring positions from the jet exit that have been measured with the Pitot rake.*

Several other measurements where also performed, but as separation occurred due to the measurement position being too close to the exit of the jet the results of these are not included. (as mentioned in chapter 2.11) Separation occurred for the measurement which were taken in what is considered the near field of the jet based on the branch point definition discussed in chapter 1.2.

3.1.1 Velocity fields

Figure 3.1 and 3.2 show the resulting velocity fields from the rake measurements at the locations $x/d_j = 20$ and $x/d_j = 30$. The contour plots show the non-dimensionalized velocity measured by the rake. All the measurements start in the center of the channel at $z = 0$, and shows the right side of the domain of the jet in cross-flow field.

The velocity increases from low velocities at the bottom region of the domain, which is highly influenced by the floor of the channel, to the center of the channel. In the figures with $V_r = 10$ and $V_r = 14$ (figures $3.1c$ and $3.2c$) the velocity is again decreasing in the upper region of the figure due to the proximity of the channel roof.

There is a region in the center of the channel (at z = 0) where there is a significant decrease in the velocity. This dip in velocity is visible in all the results from the Pitot rake measurements, and is caused by the wake behind the jet flow.

A higher flow velocity is induced by the counter rotating vortex pair associated to the JICF velocity field, with a maximum velocity in the core

center [1]. The vortex cores were expected to be seen at approximately the same height as the wake. In the results from the Pitot rake, there is not observed any significant increase in the velocity at this position.

Some of the measurements show an arc shaped region of increased velocity just above the wake (figure 3.1(c) and 3.2(c)). This occurs for the higher of velocity ratios that have been measured, and is not seen in velocity ratios below 10.

Table 3.2 lists the minimum velocity observed in the wake of the jet, together with the maximum velocity in the flow field measured by the rake.

$\mathbf{x/d_j}$	$\mathbf{V_r}$	$\mathbf{U_{min}/U_\infty}$	$\mathbf{U_{max}/U_\infty}$
20	5	0.63	1.01
20	7	0.77	1.01
20	10	0.61	1.08
30	5	0.66	1.01
30	7	0.72	1.01
30	14	0.48	1.12
40	10	0.74	1.02

Table 3.2: Minimum and maximum velocity observed for the different measurements performed with the Pitot rake

Figure 3.1: Velocity fields from rake measurements at $x/d_j = 20$ for velocity ratios: (a) $V_r = 5$, (b) $V_r = 7$ and (c) $V_r = 10$

a)

b)

c)
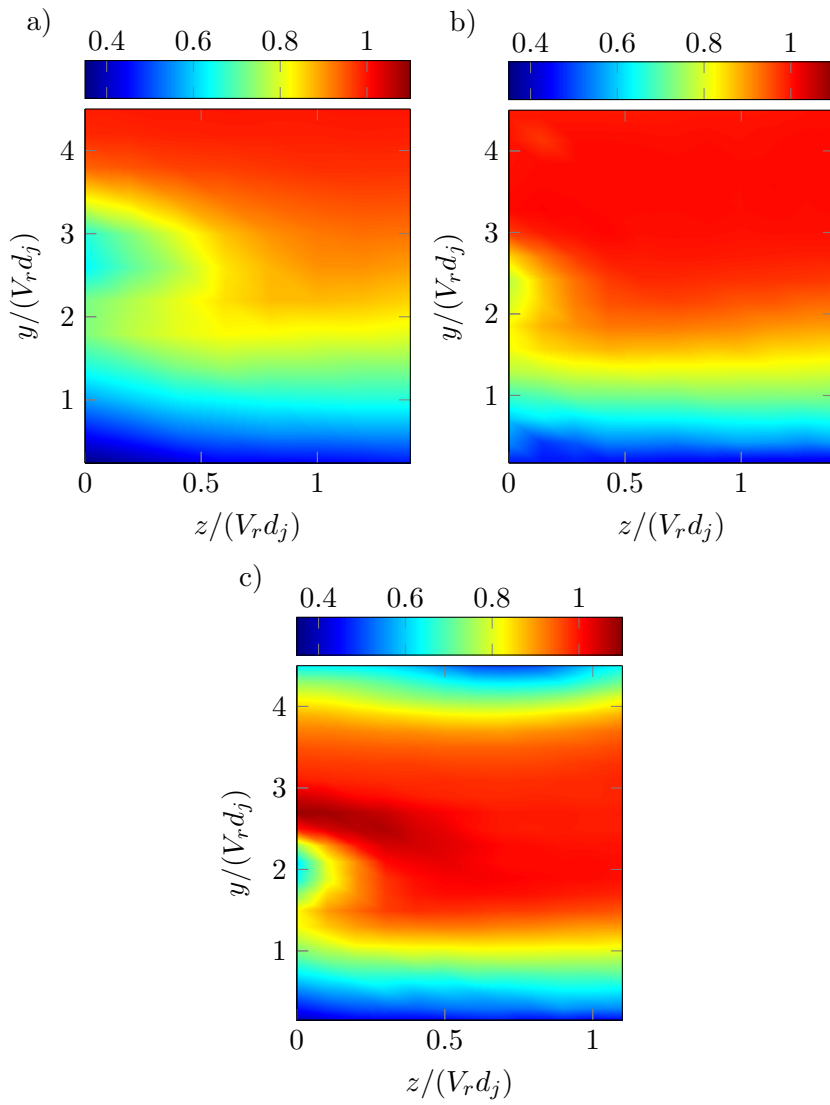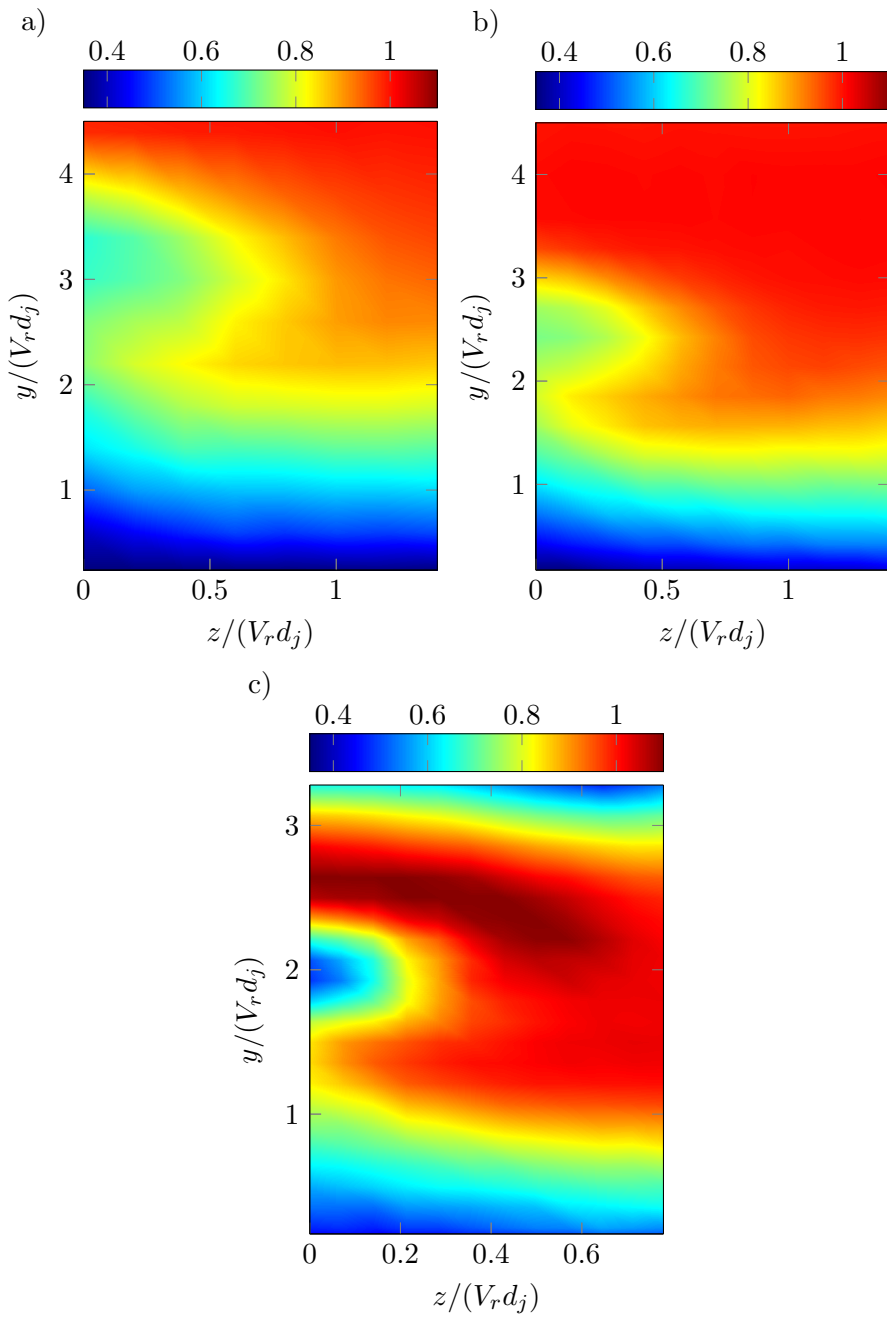

Figure 3.2: Velocity fields from rake measurements at $x/d_j = 20$ for velocity ratios: (a) $V_r = 5$, (b) $V_r = 7$ and (c) $V_r = 14$

33

3.2   5-hole Pitot probe

An overview of the different measurement positions and velocity ratios for the cases executed by the 5-hole Pitot probe is shown in table 3.3. The focus of the 5-hole Pitot measurements was on two velocity ratios (5 and 10), and the development of the jet trajectory downstream of the jet exit for these.

x/d_j	V_r	
30	5	10
40	5	10
50	5	10
60	5	10
70		10

Table 3.3: The different velocity ratios for the measuring positions from the jet exit that have been measured by the 5-hole Pitot probe.

Looking at the values in table 3.4 and 3.5 one can observe how the strength of the different velocity components varies downstream of the jet exit for the two different velocity ratios. Note that these are the measured velocities at the grid points, and that there most likely are extreme values in the flow field that have been lost due to low refinement of the grid. As there were not performed any measurements in the middle of the domain (at $z = 0$), where the minimum velocity in x-direction is expected to be found, it is difficult to say anything about the minimum velocity in wake. The values for the minimum velocities registered in x-direction are still included in table 3.4 and 3.5 to see if some trend can be noticed, and if this trend is consistent with the results from the rake.

3.2.1   Velocity fields, $V_r = 10$

The velocity fields from the different velocity components at $V_r = 10$ are presented in figures 3.3 to 3.7. Just as for the rake measurements, it is the right side of the domain that has been measured (starting from $z = 6$ mm). The exception is the measurements from the case of $V_r = 10$ at $x/d_j = 40$, which has been performed for both sides of the domain (figures 3.9-3.11). Figure 3.3 shows the development of the U_x velocity from $x/d_j = 30$ to $x/d_j = 70$. The contours of the jet vortex cores are clearly visible in the

x/d$_j$	$|U_{x,max}/U_\infty|$	$|U_{x,min}/U_\infty|$	$|U_{y,max}/U_\infty|$	$|U_{z,max}/U_\infty|$
30	1.22	1.03	0.35	0.27
40	1.14	0.92	0.43	0.21
50	1.13	0.89	0.46	0.23
60	1.10	0.95	0.40	0.18
70	1.05	0.93	0.32	0.13

Table 3.4: The maximum absolute values of the different velocity components together with the minimum wake values registered downstream of the jet exit for $V_r = 10$.

x/d$_j$	$|U_{x,max}/U_\infty|$	$|U_{x,min}/U_\infty|$	$|U_{y,max}/U_\infty|$	$|U_{z,max}/U_\infty|$
30	1.05	0.85	0.27	0.15
40	1.02	0.84	0.28	0.15
50	1.02	0.86	0.25	0.12
60	1.02	0.88	0.17	0.09

Table 3.5: The maximum absolute values of the different velocity components together with the minimum wake values registered downstream of the jet exit for $V_r = 5$.

velocity field of U_x as the velocity component is higher towards the center of the cores. As the distance from the jet exit increases, the variation in velocity from the cores compared to the free-stream decreases. It is, nevertheless, still possible to see the contours of the cores at $x/d_j = 70$.

In figure 3.5 the development of the y-component of the velocity is displayed. The velocity is positive towards the center of the domain, where the cores have an upwards rotation, and negative towards the outer part of the domain where the rotating motion of the cores is downwards. At $x/d_j = 70$ there is still a clearly visible effect from the cores to the vertical flow field. The strength of the vertical velocity component is measured to be higher at $x/d_j = 40$, 50 and 60 than for $x/d_j = 30$ (table 3.4).

The z-component of the velocity is displayed in figure 3.7. The values of the component are negative at the bottom region of the domain, and positive at the top, following the rotating motion of the vortex cores. It can be noted that the strength of the velocity component has weakened to around half the value at $x/d_j = 70$ from the earliest measurement at $x/d_j = 30$.

In figure 3.9-3.11 both the left and right side of the domain are included,

with the center of the jet at $z = 0$. The measuring positions closest to $z = 0$ is at ± 6 mm, hence the information about the center of the wake is not very accurate. In figure 3.9 the contours of the x-component of the total velocity is plotted with the vector plots the velocity parallel to the y-z plane.

3.2.2   Velocity fields, $\mathbf{V_r = 5}$

The developing velocity fields from the different velocity components at $V_r = 5$ are presented in figures 3.4-3.8.

From the results of the x-component of the total velocity (figure 3.4), an increase in the velocity reveals were the vortex cores are. This velocity increase is significantly smaller than for the measurements with a $V_r = 10$, and at $x/d_j = 60$. The local velocity increase in the vortex core center is as little as 0.26 m/s compared to the far field velocity (far field velocity = 10.60 m/s, maximum measured velocity in vortex core = 10.86 m/s).

For the y- and z-components of the velocity, the presence of the vortices are clearly evident in the flow field for all downstream positions that have been measured. The y-component of the velocity is, just like for $V_r = 10$, stronger further downstream before it starts to decrease. Furthermore the z-component has been about halved for $x/d_j = 60$ compared to $x/d_j = 30$. In the measurements of U_y (figure 3.8) more noise is observed in the measurements than for the other results. This applies for all the measurement locations starting from $x/d_j = 40$ and further downstream from the jet exit. The noise is increasing further away from the jet.

3.2.3   5-hole Pitot probe vs. Pitot rake

In figure 3.12, two results from the 5-hole Pitot probe and the Pitot rake measurements are put next to each other for a better comparison. The measurements in (a) and (b), and in (c) and (d) are from the same measurement positions and at the same velocity ratios.

3.2.4   Jet trajectory

As the vortex cores were not visible in the measurements done with the Pitot rake, the jet trajectory was followed based on the height of the center of the wake. The location of the center was decided by the position of lowest velocity in the wake. Because the resolution of the grid from the measurements was coarse, an interpolation between the grid points was performed to find the correct position of the the minimum velocity.

For the measurements done with the 5-hole Pitot probe, the jet trajectory was followed based on the height of the center of the vortex cores. The location of the vortex cores were determined by the point with the highest velocity in x-direction. The procedure with interpolation between the grid points was done also here to find the correct position of the maximum velocity.

The results were non-dimensionalized by the global length scale, $V_r d_j$, and plotted together with equation 1.17 in figures 3.13 and 3.14. The scaling constants used to fit the curve were found by using the power function in the curve fitting tool in MATLAB. The constants were found to be $A = 1.60$ and $m = 0.36$ for the wake values from the Pitot rake, and $A = 1.67$ and $m = 0.35$ based on the position of the vortex cores gotten from the 5-hole Pitot results.

Figure 3.3: The velocity contours of the development of U_x for $V_r = 10$ at the downstream positions $x/d_j = 30, 40, 50, 60$ and 70.

Figure 3.4: The velocity contours of the development of U_x for $V_r = 10$ at the downstream positions $x/d_j = 30, 40, 50$ and 60.
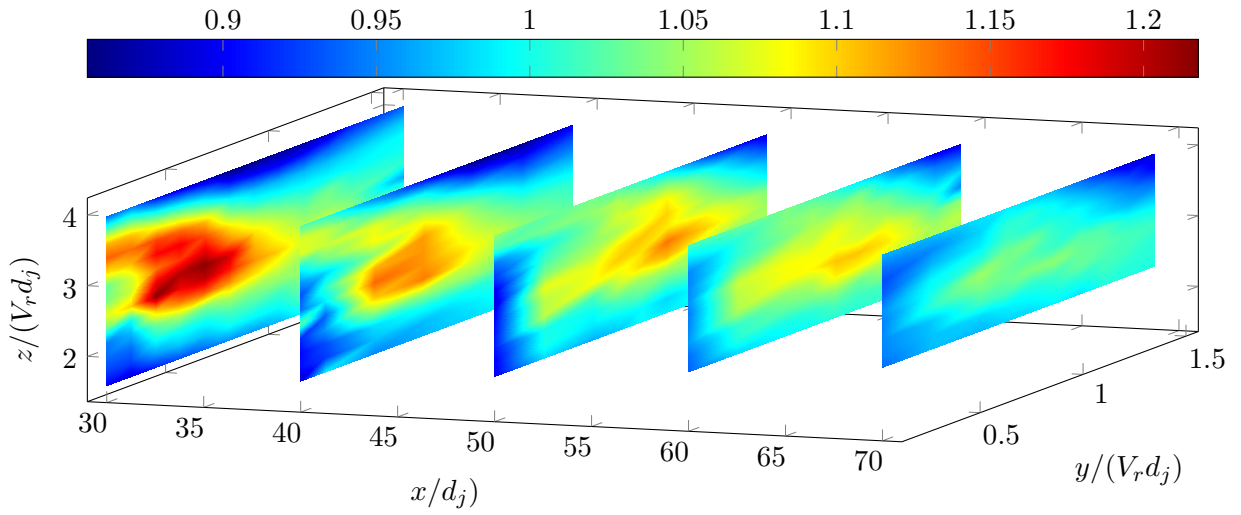
Figure 3.5: The velocity contours of the development of U_y for $V_r = 10$ at the downstream positions $x/d_j = 30, 40, 50, 60$ and 70.

Figure 3.6: The velocity contours of the development of U_y for $V_r = 10$ at the downstream positions $x/d_j = 30, 40, 50$ and 60.
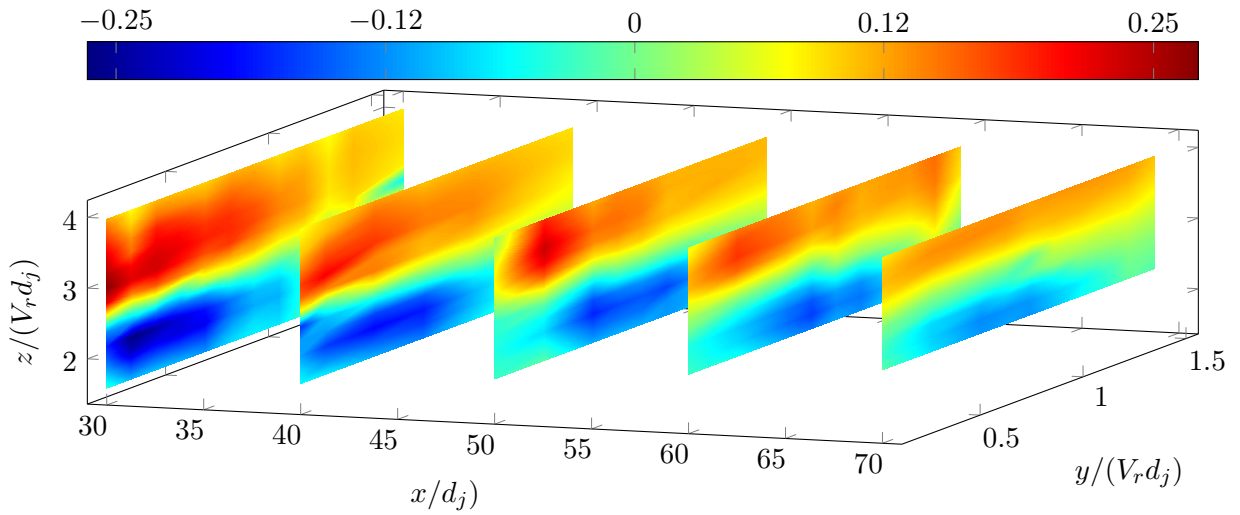
Figure 3.7: The velocity contours of the development of U_z for $V_r = 10$ at the downstream positions $x/d_j = 30, 40, 50, 60$ and 70.
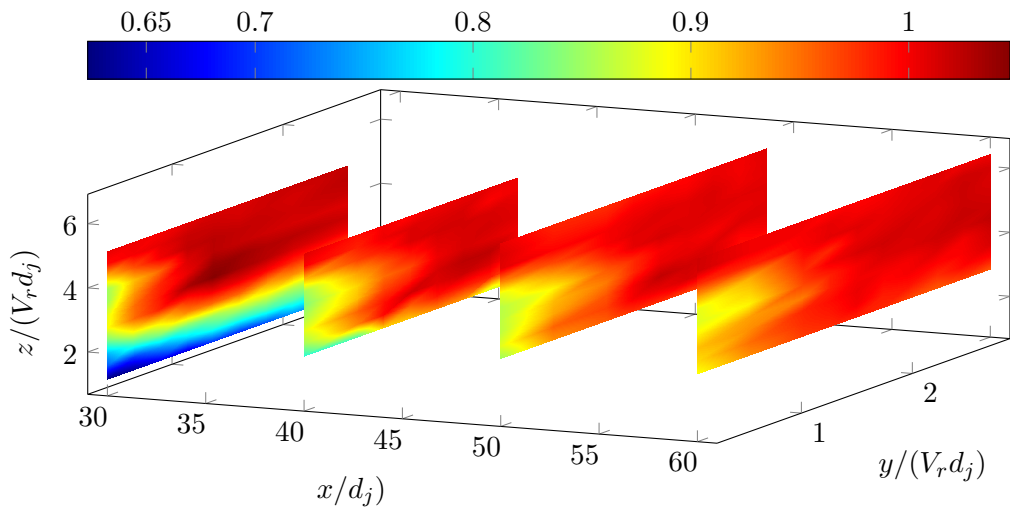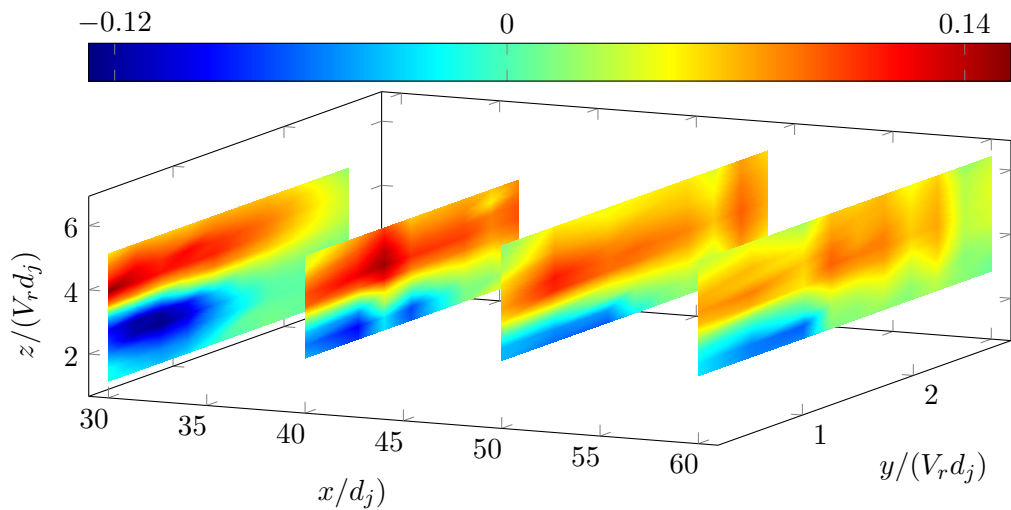

Figure 3.8: The velocity contours of the development of U_z for $V_r = 10$ at the downstream positions $x/d_j = 30, 40, 50$ and 60.
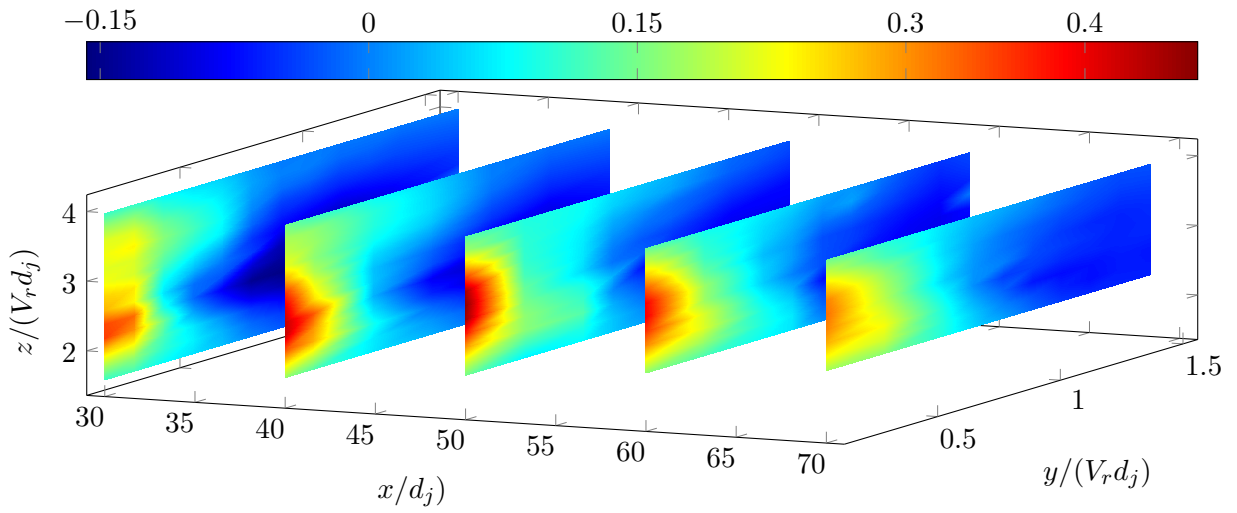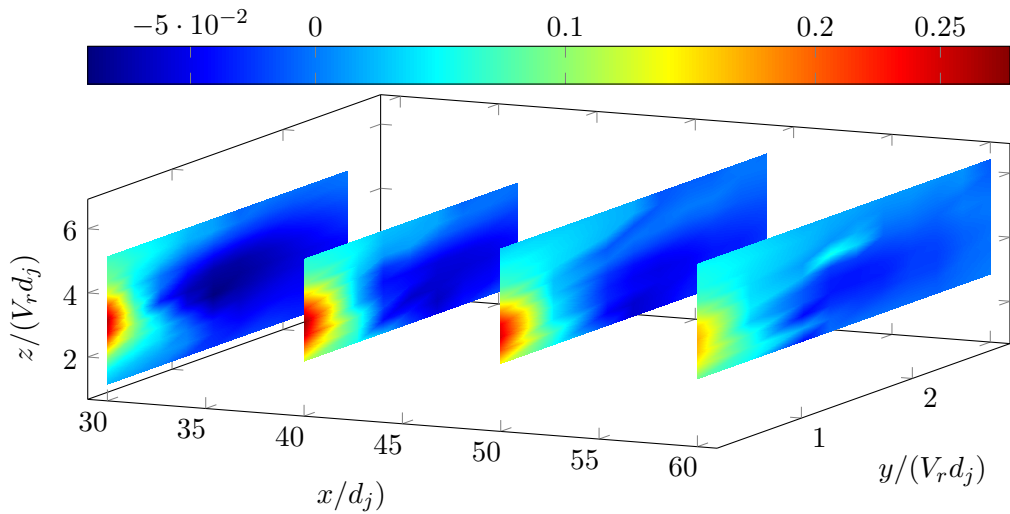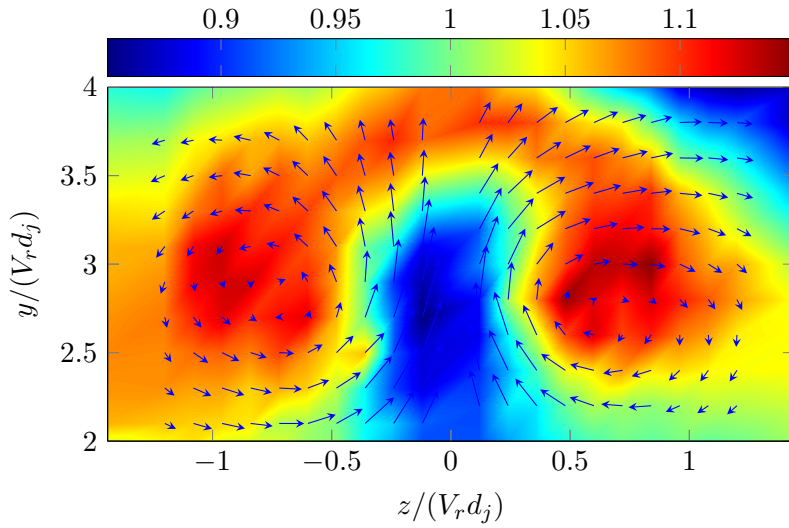
Figure 3.9: Velocity contours of U_x for $V_r = 10$ at $x/d_j = 40$, with the vector plots the velocity parallel to the y-z plane.
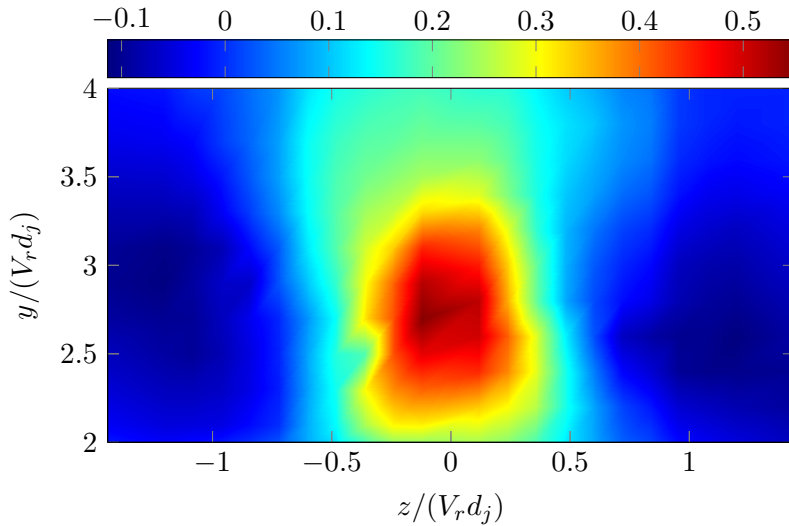
Figure 3.10: Velocity contours of U_y for $V_r = 10$ at $x/d_j = 40$.
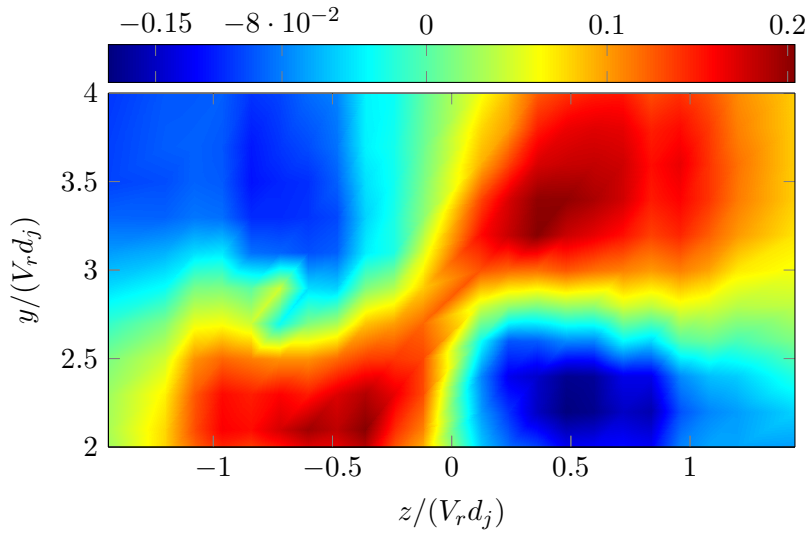
Figure 3.11: Velocity contours of U_z for $V_r = 10$ at $x/d_j = 40$
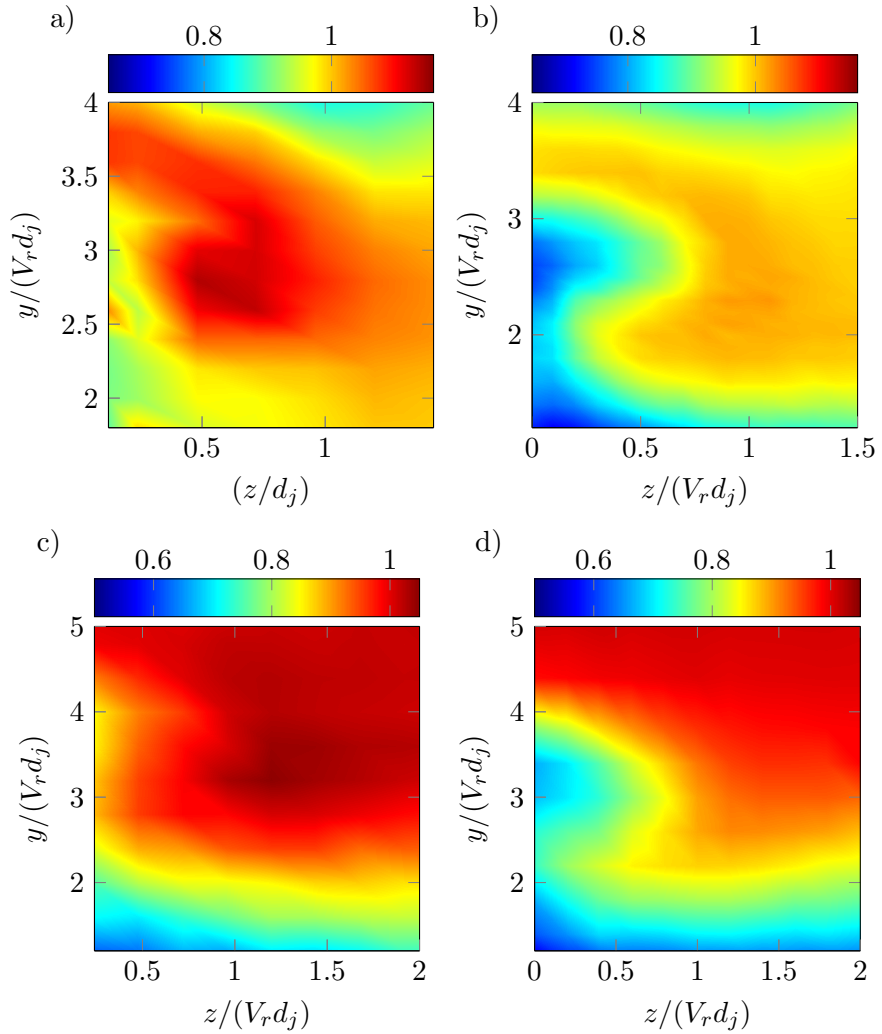
Figure 3.12: Comparison of 5-hole Pitot probe measurements (left) and Pitot rake measurements (right) for $V_r = 10$, $x/d_j = 40$ (a, b), and $V_r = 5$, $x/d_j = 30$ (c, d).
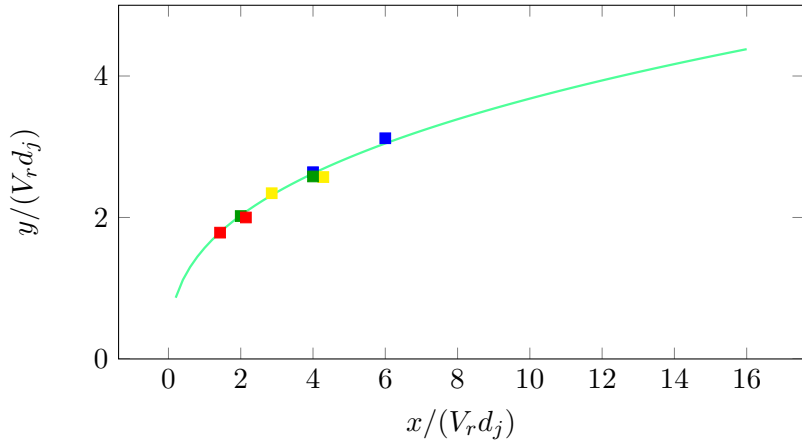
Figure 3.13: Jet trajectory based on core height from rake results for the velocity ratios: ■ *: $V_r = 5$,* ■ *: $V_r = 7$,* ■ *: $V_r = 10$,* ■ *: $V_r = 14$ and* —— *: calculated trajectory with scaling constants $A = 1.60$ and $m = 0.36$.*
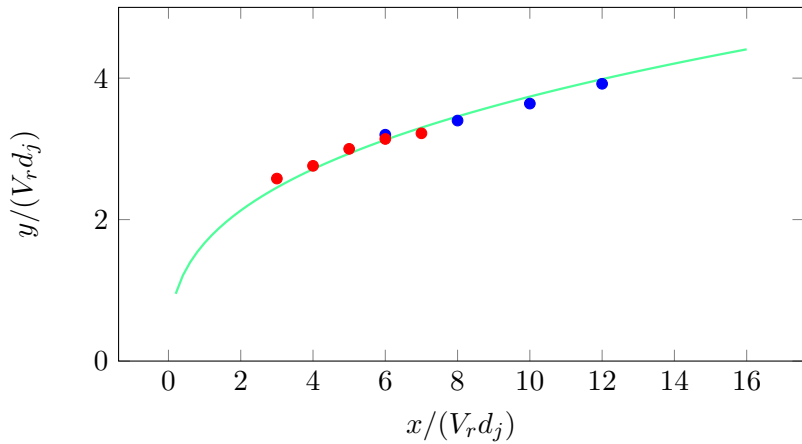
Figure 3.14: Jet trajectory based on core height from 5-hole Pitot results for the velocity ratios: ● *: $V_r = 5$,* ● *: $V_r = 10$ and* —— *: calculated trajectory with scaling constants $A = 1.67$ and $m = 0.35$.*

Chapter 4

Discussion

4.1 Velocity fields

The resulting contour plots of the velocity fields based on the Pitot rake results (figures 3.1, 3.2 and 3.12(b) and (d)) differ from the velocity field from the 5-hole Pitot probe result (figures 3.3-3.3 and 3.12(a and (c)) in several manners, discussed in the following sections.

4.1.1 Comparison of results from the Pitot rake and the 5-hole Pitot probe

Vortex cores

When studying figure 3.12, one see that the differences in the flow picture are bigger for the results of a velocity ratio of 10 (figure 3.12 (a) and (b)). In the results from the Pitot rake results there are no significant increase in the velocity in the region next to the wake of the jet, where the vortex cores are assumed to be, whereas for the 5-hole Pitot measurements, the contours of the cores are visible in this region.

Looking at table 3.2, the maximum velocity measured in the flow field does not exceed $U_{max}/U_\infty = 1.02$ for the cases which does not have the arc shaped region of higher velocity above the wake.

For comparison, the values for the maximum velocity in x-direction, $U_{x,max}/U_\infty$, gotten from the 5-hole Pitot probe for the same velocity ratio, at the same downstream positions in the channel as the rake measurements are in the area of 1.14-1.22 (see table 3.4) The 5-hole Pitot probe has thus registered a velocity in x-direction which is significantly higher than the velocity registered with the Pitot rake.

For a velocity ratio of 5, the contours of the vortex core are not as visible in the 5-hole Pitot probe measurements as for the results with a velocity ratio of 10. However, there is still a noticeable increase in the velocity determining the position of the vortex core.

The wake

As for the minimum velocities registered in the wake measured by the rake, it is hard to know if this is the actual correct values as the probe has proven to give incorrect results for other parts of the velocity field. The trend, however, shows that a higher velocity ratio gives a higher velocity in the center of the wake. It also shows that further downstream from the jet the velocity inside the wake has increased, as the jet-flow becomes more uniform with the surrounding cross-flow. (table 3.2)

The exception is the measurement of velocity ratio 14 at downstream position $x/d_j = 30$. As the velocity ratio is high, the far field has still not started at this position. According to equation 1.4, the branch point of a JICF with a velocity ratio of 14 is at $39.2d_j$. At $x/d_j = 30$ the jet has hence probably not had the necessary time to be bent fully over in the direction of the cross-flow yet. It has, however, had time to bend enough not to get full flow separation when encountering the probes. This can explain the deviation in these particular results from the rest of the Pitot rake results which are all taken from the far field of the jet.

It is hard to make a statement about the development of the wake for the measurements done with the 5-hole Pitot probe as the center-position of the jet (and hence the expected center of the wake) was not measured. Based on the values in table 3.4 and 3.5 for the minimum velocity found in the wake region, there is no clear trend in the results for $V_r = 10$; the registered minimum values are first decreasing, then increasing.

For $V_r = 5$ the minimum values in the wake are more or less constantly increasing when moving further away from the jet exit. This fits well with what is observed from the Pitot rake measurements.

Explanations why the results from the velocity ratio of 10 is varying so randomly can be that the points of the lowest velocity have been missed when doing the measurements due to the relatively coarse grid, or because the measurements are taken too far from the actual center of the wake, and thus the trend has disappeared.

Something else to notice is that the area of low velocity due to the wake seems to be greater in span wise direction in the results from the Pitot rake (figure 3.12). This might be caused by wrongly measured values by the

Pitot rake.

4.1.2 5-hole Pitot probe: Comparison of $V_r = 10$ and $V_r = 5$

Compared to the results from the $V_r = 10$ measurements, the trend of the results from the $V_r = 5$ measurements is similar.

For the x-component of the velocity, the vortex cores are more visible in the $V_r = 10$ case. Because the initial velocity difference is smaller in the $V_r = 5$ measurements, it is expected that the jet flow will sooner be uniform with the cross-flow, and thus the contours of the vortex cores should be stronger in the results of $V_r = 10$.

The values of the vertical velocity is almost doubled in the $V_r = 10$ case compared to results for the $V_r = 5$ case. This is reasonable as the initial velocity of the jet is vertical, and the jet has a higher initial value for the $V_r = 10$ case.

Noise in the measurements for the z-component of the velocity at $V_r = 5$ is registered in the resulting contour plot. A reason for this can be that the difference in velocity is small (a variation in U_z/U_∞ from -0.056 to 0.095 at $x/d_j = 60$), and the probe has not been able to measure the correct velocity in a way accurate enough to get smooth results.

4.1.3 Comparison with PIV measurements

Figure 4.1 is from [1], and shows the mean velocity fields of the velocity components U_x, U_y and U_z in a JICF based on Particle Image Velocimetry (PIV) measurements. The velocity ratio is 10, and the downstream positions from the jet exit are $30d_j$, $55d_j$ and $85d_j$.

Pitot rake

Comparing these results with the results from the Pitot rake, it is clear that several typical flow characteristics associated with the jet in cross-flow are absent in the flow picture generated by the rake. There is, for instance, no sign of the counter rotating vortices in most of the results. Looking at the plots of U_x in figure 4.1, the center of the vortex cores are almost aligned with the center of the wake. The arc shaped region which is found above the wake in the results from $V_r = 10$ and $V_r = 14$ (figures 3.1c and 3.2c), is also seen in the PIV results at $x/d_j = 30$. It could be that this is the jet which is still being bent over by the cross-flow, and thus the CVP has not fully developed yet, as the measurements are done close to the near field

of the jet, determined by x_{bp}. The fact that this arc shaped region of high velocity is only visible in the measurements with higher velocity supports this as the branch point is moved further downstream with higher velocity ratios (equation 1.4).

The poor results from the Pitot rake is caused because the probes of the rake are only able to measure the total velocity of the flow in the direction they are aligned with a good accuracy up to±11° [16]. If the incoming flow is at a different angle then the probe, the pressure applied to the pressure taps of the Pitot rake will not be the total pressure. As the flow field of the JICF is complex and the inlet angle of the flow on the probes is far from constant, the probes do not manage to catch the correct velocity in the areas where the CVP is dominant. Hence the CVP will not be visible in the resulting flow field.

5-hole Pitot probe

The velocity fields gotten from the 5-hole Pitot probe for a velocity ratio of 10 (figures 3.3 to 3.7) show a similar behaviour as the PIV results.

At $x/d_j = 30$ the maximum x-velocity in the center of the cores seem to be in the same order of magnitude for both the 5-hole Pitot probe and the PIV measurements (slightly above 1.2). The same is the case for the span wise velocity component, U_z, where the maximum velocity magnitude is in the region around $U_y/U_\infty = 0.25$. The maximum velocity of the vertical velocity component is greater in the PIV measurements (0.35 compared to around 0.7 from the PIV results), but as the highest value is expected to be found in the middle of the domain ($z = 0$), and this section did not get measured with the 5-hole Pitot, this might be the explanation for the deviation.

When moving downstream from the jet exit the increase of U_x in the vortex core center is fading out for both the PIV and the 5-hole Pitot measurements. At $V_r = 10$, $x/d_j = 60$ (figure 3.3) the arc region is still visible in the flow field, even though the branch point for this case is at $x_{bp} = 20d_j$, and the CVP at this point should be fully developed. In the PIV measurements for $x/d_j = 50$, there is no signs left of this arc region. This implies that the development of the CVP might be delayed in the turbulent channel flow.

Another difference that is observed between the two sets of results is the shape of the vertical velocity field (U_y). In figure 4.1(c) one can see that the region with increased velocity is not completely elliptical but covers a greater area towards the sides at the bottom of the region. This uneven-ness, however, disappears further downstream and is no longer visible at
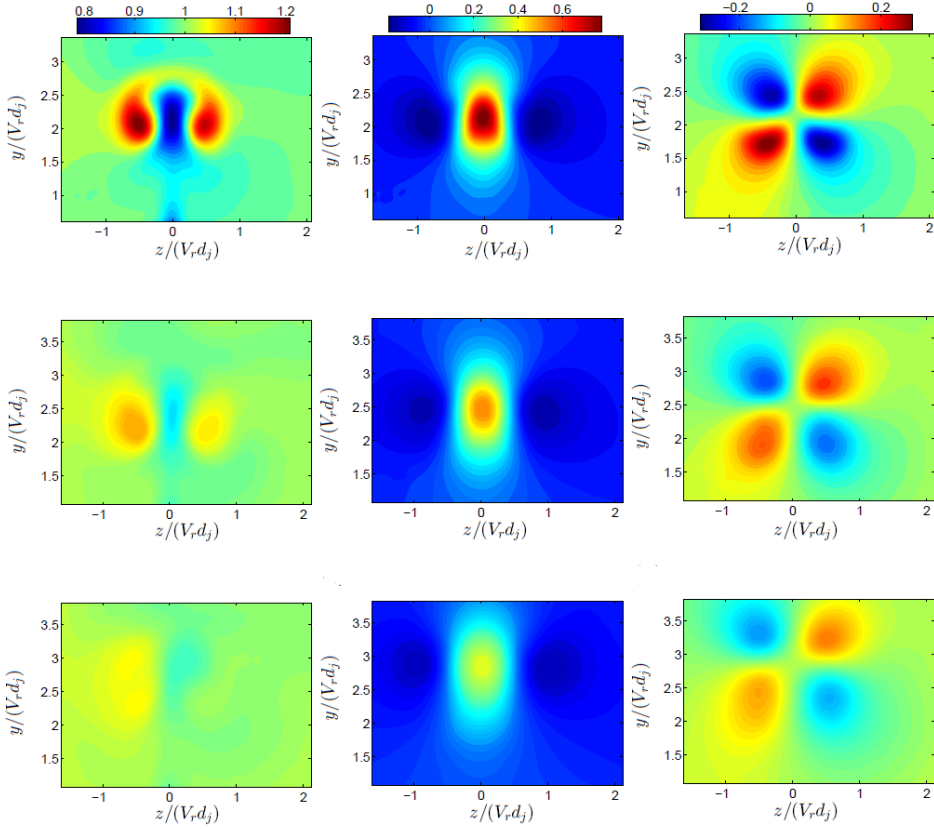
Figure 4.1: The mean velocity field for $V_r = 10$, from [1]. U_x/U_∞, U_y/U_∞ and U_z/U_∞ are plotted from left to right for the downstream positions: $x/d_j = 30$ (a to c), $x/d_j = 55$ (d to f) and $x/d_j = 85$ (g to i)

$x/d_j = 50$. In the 5-hole Pitot results, this region of increased is more evident and visible even at $x/d_j = 70$ for $V_r = 10$. The positive vertical velocity in the proximity of the channel floor might be the cause of this occurrence (figure 2.6).

In figure 4.2 the results from [1] and the from the measurements with the 5-hole Pitot probe (also shown in figure 3.9-3.11) are positioned next to each other for a better comparison. The results are all taken from a velocity ratio of 10. The PIV measurements (figure 4.2 (a)-(c)) are taken from a downstream position of $x/d_j = 30$, while the 5-hole Pitot probe measurements (figure 4.2 (d)-(e)) are from $x/d_j = 40$. As the measurements from

the 5-hole Pitot probe is taken further downstream, the jet trajectory has had time to develop further, and penetrate deeper into the flow.

The shape of the cores for the various velocity components are similar for the two results. The contour plots from the PIV measurements are much smoother, most likely due to a more refined grid during the measurements. Another reason for the smoother results can be the fact that during PIV measurements, there is nothing that is interfering with the flow. Even though the 5-hole Pitot probe is small, it is still present within the flow and will cause some disturbance.

There are some asymmetric occurrences in the flow field of the different velocity components from both the PIV measurements and the 5-hole Pitot probe measurements. In the U_x contours one of the cores of the CVP has expanded more than the other both in figure 4.2 (a) and (d).

In the results of U_x, the arc shaped region of higher velocity connecting the cores is again much more visible in the 5-hole Pitot probe measurements, despite the fact that the results are taken from further downstream, and it is expected that the CVP should be fully developed.
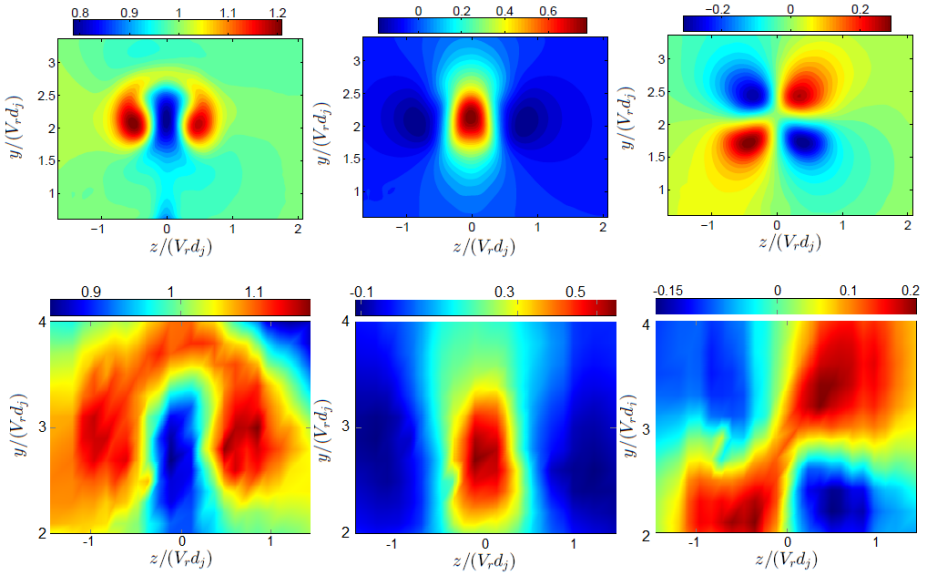

Figure 4.2: The mean velocity field for $V_r = 10$, from [1] at $x/d_j = 30$, and from the 5-hole Pitot measurements at $x/d_j = 40$. U_x/U_∞, U_y/U_∞ and U_z/U_∞ are plotted from left to right.

4.2 Scaling of the jet trajectory

The graphs in figure 3.13 and 3.14 show that the measured points and the calculated line for the trajectory are collapsing well, both for the rake and the 5-hole Pitot measurements. Some of the points are a slightly off the line, but overall the match is good.

The values chosen to fit the points from the experiments in the turbulent channel flow is within the interval of acceptable values for A and m from chapter 1.2.1. The derived value of m is $1/3$. 0.35 and 0.36 are both quite close to this derived value.

The values used for the scaling constants in [1] were $A = 1.58$ and $m = 0.28$, thus are both the scaling constants have a lower value than the scaling constants found for the experiments in the turbulent channel flow. Hence, the scaled jet trajectory of the jet in the turbulent channel flow extends further up in the channel than the jet investigated in [1]. A reason for this can be the positive vertical velocity component in the region close to the channel floor that helps pull the jet trajectory deeper into the cross-flow. (figure 2.6)

4.3 Uncertainty analysis

There are several sources of uncertainty in this study. For the pressure measurements there might be deviations from the actual value due to incorrect measurements of the various pressures. There can be several causes for this, such as:

- Badly aligned tube in accordance with the flow. This will expose the static tubes of the Pitot static tube to some velocity component, and for the 5-hole Pitot probe the measured direction and magnitude of the flow will be wrong.

- The total pressure is proportional to the square of the velocity. Integrating this over the orifice of the Pitot tube will result in a higher value than the stagnation pressure calculated from the square of the average velocity at the geometrical center of the orifice [17].

- Deflection of stream lines in the region of low velocity due to the presence of the probe [17].

In addition to this, there is a possibility that the different probes of the Pitot rake was not perfectly aligned in the flow. Hence the measurement

positions that are actually being measured will not be the same as the positions that are believed to be measured.

Another uncertainty in the measurements lays within the positioning of the probe. The initial placement of the probe was done manually, as accurately as possible. Nevertheless, since the channel was narrow and hence the probe was hard to get to, it was difficult to determine the exact position of the probe. As for the traversing of the probes, this was also done manually, and thus there are possibilities that some errors have occurred during the process of moving the probes.

Since the measurement periods were long, the ambient conditions in the laboratory were likely to undergo some changes during this period. For instance some changes in the atmospheric pressure was observed when the door of the laboratory was open at the same time as the door going out. If this happened during the sampling time of a measurement, it would cause some errors in the results.

Chapter 5

Conclusion

The velocity field based on the rake results (figures 3.1 and 3.2) are lacking essential information about the flow structure. Main characteristics of the jet in cross-flow, such as the CVP are lost in the measurements, and the only sign of the jet which is left in most of the contour plots based on the Pitot rake results is the wake behind the jet. The Pitot rake can thus be considered as unfit to perform measurements of the jet in cross-flow. Nevertheless, as seen in chapter 3.2.4, the information about the location of the wake can still be used to follow the jet trajectory. Thus if the only interest is to follow the development of the trajectory, using the Pitot rake could be an option as it is less time consuming to perform measurements with the rake than with the 5-hole Pitot.

The results based on the measurements performed with the 5-hole Pitot show a good agreement with the PIV results from [1]. The value of the different velocity components are in the same order of magnitude, and the contour plots have a similar appearance. As the grid refinement is not very good for the 5-hole Pitot measurements compared to the PIV measurements, some information about the flow is lost. Hence it is difficult to accurately state the exact position and value of the center of the vortex cores.

These issues can be solved by acquiring a more sophisticated traverse system and/or additional 5-hole Pitot probes which can be mounted on a rake. This would make the measurements more efficient, and increase the accuracy.

Based on the results gotten from this study, it the roughness on the channel floor does not seem to have a great effect on the development of the flow field behind the jet. There appears to be some influence on the flow due to the proximity of the walls such as an increased vertical velocity component

(see chapter 4.1.3 and 4.2).

There are also signs that suggest that the development of the cores might be somewhat delayed in the channel flow. (see chapter 4.1.3)

It is not known how the instantaneous flow structures of the flow discussed in chapter 1.2 are effected by the turbulent channel flow, as it is only the averaged behaviour which is captured by the pressure probes. It is, however, probable that these structures are influenced by the boundary layer.

Bibliography

[1] N. Lanitis and J. Dawson. An experimental study of the turbulent structure in the far field of a jet in cross-flow. part 1. statistical description. *J Fluid Mech.*, 2015.

[2] Krishnan Mahesh. The interaction of jets with crossflow. *Annu. Rev. Fluid Mech. 2013*, 2013.

[3] Ann R. Karagozian. Transverse jets and their control. *Progress in Energy and Combustion Science*, 2010.

[4] Krishnan Mahesh. The interaction of jets with crossflow. *Annual Review of Fluid Mechanics*, 2012.

[5] Y. Kamotani and I. Greber. Experiments on a turbulent jet in a cross flow. *AIAA Journal 10:11, 1425-1429*, 1972.

[6] T. T. Lim A. E.Perry, R. M. Kelso. Topological structure of a jet in a cross flow. *AGARD, Computational and Experimental Assessment of Jets in Cross Flow*, 1993.

[7] S. H. Smith and M. G. Mungal. Mixing, struture an scaling of the jet in crossflow. *J Fluid Mech*, 1997.

[8] A. R. Karagozian L. S. Alves, R. E. Kelly. Transverse-jet shear-layer instabilities. part 2. linear analysis for large jet-to-crossflow velocity ratio. *J Fluid Mech.*, 2008.

[9] R. L. Fearn and R. P. Weston. Induced velocity field of a jet in a crossflow. *NASA Technical paper 1087*, 1978.

[10] J. F. Keffer and W. D. Baines. The round turbulent jet in a cross-wind. *J Fluid Mech.*, 1963.

[11] B. D. Pratte and W. D. Baines. Profiles of the round turbulent jet in a cross flow. *J. Hydraul. Div.*, 1967.

[12] Y. Kamotani and I. Greber. Experiments on turbulent jet in a cross-flow. *AIAA J.*, 1972.

[13] J. E. Broadwell and R. E. Breidenthal. Structure and mixing of a transverse jet in incompressible flow l. *J Fluid Mech*, 1984.

[14] J. R. Dawson and T. B. Nickels. Boundary layer theory. *Incompressible Flow*, 2007.

[15] Frank M. White. *Viscous Fluid Flow*. McGRAW HILL International Edition, 3rd edition, 2006.

[16] Boerrigter Buchlin Carbonaro Degrez Dnos Fletcher Olivari Riethmuller Anthoine, Arts and Van den Braembussche. *Measurement techniques in fluid dynamics*. Von Karman Institute for Fluid Dynamics, 1640 Sint-Genesius-Rode, Belgium, 3rd edition, 2009.

[17] Ernest O. Doebelin. *Measurement Systems application and design*. McGRAW-HILL International Editions, Palo Alto, 4th edition, 1990.

[18] M. T. Schobeiri G.L. Morrison and K.R. Pappu. Five-hole pressure probe analysis technique. *Flow Measurement and Instrumentation.*, 1998.

[19] Heiner Schumann. The interaction between wind turbines caused by their respective wakes. *Technische Universitt Darmstadt*, 2012.

[20] Lambrecht meteo. http://lambrecht.net/de/weitere-parameter/luftdruck/13/mikro-manometer–655-. Accessed: 2015-09-06.

[21] *Bruksanvisning for påk SCANIVALVE CONTROLLER.*